Modeling of the Dec. 22nd 2018 Anak Krakatau volcano lateral collapse and tsunami based on recent field surveys: comparison with observed tsunami impact

Grilli[1] S.T., Zhang[2] C., Kirby[2] J.T., Grilli[1] A.R., Tappin[3,4] D.R., Watt[5] S.F.L., Hunt[6], J.E., Novellino[3], A., Engwell[3] S., Nurshal M.E.M.[7], Abdurrachman M.[7], Cassidy, M.[8], Madden-Nadeau A.L.[8] and S. Day[4]

1. Department of Ocean Engineering, University of Rhode Island, USA
2. Center for Applied Coastal Research, University of Delaware, USA
3. British Geological Survey, Nottingham, UK
4. University College, London, UK
5. School of Geography, Earth and Environmental Sciences, University of Birmingham, UK
6. National Oceanography Centre, Southampton, UK
7. Bandung Institute of Technology, Indonesia
8. Department of Earth Sciences, University of Oxford, UK

Abstract

The Dec. 22, 2018 lateral collapse of the Anak Krakatau (AK) volcano in the Sunda Straits of Indonesia discharged volcaniclastic material into the 250 m deep caldera southwest of the volcano and generated a large tsunami, causing runups of up to 85 m in the near-field, and 13.5 m in the far-field, on the nearby coasts of Sumatra and Java. The tsunami caused 437 fatalities, the greatest number from a volcanically-induced tsunami since the catastrophic explosive caldera-forming eruption of Krakatau in 1883 and the sector collapse of Ritter Island in 1888. For the first time in over 100 years, the 2018 AK event provides an opportunity to study a major volcanically-generated tsunami that caused widespread loss of life and significant damage. Here, we present numerical simulations of the collapse and tsunami generation, propagation, and coastal impact, with state-of the-art numerical models, using both a new parametrization of the collapse and a near-field

bathymetric dataset based on our 2019 field surveys and satellite images. These subaerial and submarine data sets are used to constrain the geometry and magnitude of the landslide mechanism, which show that the primary landslide scar bisected the AK edifice, cutting behind the central vent and removing 50% of its subaerial volume. The primary landslide volume is estimated to range from 0.175 – 0.313 km^3, based on uncertainties in the shape of the submerged part of the failure plane. This is supported by an independent estimate of the primary landslide deposit volume of 0.214 ± 0.036 km^3. Given uncertainties in the failure volume, we define a range of potential failure surfaces that span these values in 4 collapse scenarios of volume ranging from 0.175 to 0.313 km^3. These AK collapses are modeled, assuming either a granular or viscous fluid rheology, together with their corresponding tsunami generation and propagation. Observations of a single tsunami, with no subsequent waves, are consistent with our interpretation of landslide failure in a rapid, single phase of movement rather than a more piecemeal process, generating a tsunami which reached nearby coastlines within ~30 minutes. For both modelled rheologies, the 0.224 km^3 collapse (second and preferred scenario) most successfully reproduces the near- and far-field tsunami flow depth and runup observed in all post-event field survey results, tide gauge records, and eyewitness reports to date, suggesting our estimated landslide volume range is appropriate. This event highlights the significant hazard posed by relatively small-scale lateral volcanic collapses, which can occur *en-masse*, without any precursory signals, and are an efficient and unpredictable tsunami source. Our successful simulations demonstrate that current numerical models can accurately forecast tsunami hazards from these events. In cases such as Anak Krakatau's, the absence of precursory warning signals, together with the short travel time following tsunami initiation present a major challenge for mitigating tsunami coastal impact, stressing the need to develop and install early warning systems for such events.

1 Introduction

Over the past 20 years, catastrophic tsunamis in Papua New Guinea (1998), the Indian Ocean (2004), and Japan (2011) have led to major advances in understanding and modeling tsunamis from submarine landslides, earthquakes, and dual mechanisms. These advances have mainly focused on improving constraints on these recent events and their geographical distribution, together with improved numerical tsunami modelling capability (e.g., Tappin et al., 2008; Grilli et al., 2007; Ioualalen et al., 2007; Grilli et al., 2013; Kirby et al., 2013; Tappin et al., 2014; see Yavari-Ramshe and Ataie-Ashtiani, 2016, for a recent review). Tsunamis from volcanic eruptions and collapses remain less well-studied because, up until recently, there were few well-recorded and researched events. However, they have the potential for generating mega-tsunamis (Paris et al., 2020b), resulting in significant loss of life and property (Day, 2015; Paris, 2015), and they account for approximately 20% of all volcanic fatalities over the past 400 years (Auker et al., 2013).

Most known lateral collapse events at volcanic islands are prehistoric, and their tsunami generation is inferred from the distribution of their submarine deposits rather than being based on direct observations. In some cases, elevated boulder deposits provide supporting evidence of extreme wave heights being produced by these collapses (e.g., Paris et al., 2020b). Many such events were large-volume (> 10 km^3) lateral volcanic collapses of ocean islands above mantle plumes, such as in the Canary Islands (e.g., Ward and Day, 2001; Day et al., 2005; Løvholt et al., 2008; Abadie et al., 2012; Giachetti et al., 2012) and Hawaii (e.g., McMurty et al., 2003). In contrast, some were smaller scale events on subduction zone volcanoes, including historical edifice collapses such as those at Ritter Island 1888 (5 km^3; Ward and Day, 2003) and Stromboli 2002 (0.01 km^3; Tinti et al., 2006; Fornaciai et al., 2019). Of historical events, the best studied eruption-

generated tsunami is that at Krakatau, Indonesia in 1883 (Verbeek, 1983, 1885; Simkin and Fiske, 1983; Siswowidjoyo, 1983). During theis eruption, there were 19 tsunamis, with the most destructive generated during the final, cataclysmic, caldera collapse and the associated emplacement of pyroclastic flow material into the sea, which destroyed the volcanic edifice and caused 33,000 fatalities (Simkin and Fiske, 1983). Another highly destructive volcanic tsunami was generated by the lateral collapse of Ritter Island in 1888. This ~5 km^3 flank collapse is the largest recorded volume lost from an island volcano in a single event in historical times (Ward and Day, 2003; Karstens et al., 2019; Watt et al., 2019). The death toll in the Ritter tsunami is poorly constrained, with the highest estimate being about 3,000 deaths (Johnson, 1987). Due to the paucity of data on most volcanic events, the results of their tsunami modelling have not been fully validated and both landslide source mechanisms (e.g., Hunt et al., 2011; Ward and Day, 2003; Watt et al., 2019) and the generated tsunamis (e.g., Day et al., 2005; Løvholt et al., 2008; Giachetti et al., 2011; Abadie et al., 2012, 2020; Tehranirad et al., 2015; Paris, 2015), remain poorly documented, so are a challenge to model. Any tsunamigenic volcanic collapse thus provides an opportunity to improve our understanding of coupled flank-failure and tsunami-generating processes, and to test and develop current landslide-tsunami numerical models. As the largest volcanic-island lateral collapse since that at Ritter Island in 1888, and with more detailed observations of both the collapse and the generated tsunami, the failure of Anak Krakatau (AK) volcano, Indonesia, in December 2018 provides important new insights that advance our general understanding of volcanic tsunamis. With remarkable prescience, Giachetti et al. (2012) modeled a tsunami from a collapse of the SW flank of the Anak Krakatau volcano, similar to that of Dec. 28th 2018, using a hypothetical 0.28 km^3 volume. The resulting wave heights and arrival times along surrounding coastlines foreshadowed the 2018 event.

In the evening of December 22, 2018, at 20:55-57 local time (Walter et al., 2019), following a 6 month period of relatively heightened eruptive activity, a lateral collapse occurred on the southwest flank of the AK volcano in the Sunda Strait, Indonesia (Figs. 1 and S1). The collapse generated a tsunami that impacted the adjacent coastlines of Java and Sumatra within 30 minutes (Grilli et al., 2019), causing up to 13.5 m runups and resulting in 437 fatalities, 13,000 people injured, 33,000 displaced and thousands of buildings destroyed (AHA, 2018; Andersen, 2018; Muhari, 2018, 2019; Grilli et al., 2019; TDMRC, 2019). The AK event was the most damaging volcanically-generated tsunami since the 1883 eruption of Krakatau and the 1888 lateral-collapse of Ritter Island. The numerous observations of AK's 2018 collapse and tsunami, including those previously unpublished by the authors of this paper, provide a unique dataset for both understanding this event and testing state-of-the-art tsunami modelling methodologies against direct observations, with the modelling constrained by both volcanic tsunami source parameters and observations of the generated waves and their coastal impact.

Here, we develop volcanic lateral-collapse scenarios based on new data from our 2019 subaerial and submarine surveys at AK (Hunt et al., 2021; Priyanto et al., 2021), model both the resulting slides and tsunami generation, and compare the latter with data from near- and far-field surveys of tsunami inundation and runup.. In our approach, the marine geology surveys inform the slide and tsunami simulations, which in turn through comparison with tsunami data help confirm the likeliest collapse scenario.

Published subaerial data on the collapse (e.g., Williams et al., 2019; Novellino et al., 2020; Perttu et al., 2020) has provided the basis for previous tsunami modelling (e.g., Grilli et al., 2019). The new numerical modeling presented hereafter is also based on this remote (mainly satellite) subaerial data but also, for the first time, on a hydroacoustic data set of multibeam echosounder

(MBES) bathymetry and seismic reflection data acquired to the southwest of the volcano after AK's eruption, in August 2019 (Hunt et al., 2021; Priyanto et al., 2021).

An important aspect of our new modelling of the 2018 collapse and tsunami generation is the use of the latest version of the three-dimensional non-hydrostatic model NHWAVE (Zhang et al., 2021a,b). This model features effects of vertical accelerations, not just in the water (as in earlier implementations) but also within the slide material itself. Our earlier modelling of the event had neglected vertical acceleration (i.e., non-hydrostatic) effects within the slide layer (Grilli et al., 2019); this was also the case in other modeling studies of this event that are detailed later. We show that including these effects is important for an accurate simulation of both wave generation from the collapse and the near-field runups. These new simulations are also performed at a much higher resolution, owing in part to the new high-resolution bathymetric and topographic data from our 2019 field survey and its subsequent analyses and reconciliations with the subaerial observations (Hunt et al., 2021). Model results for both the near- and far-field tsunami generation, propagation and coastal impact are validated against time series of sea surface elevation recorded at tide-gauges in the Sunda Straits together with all published field observations and eyewitness accounts to date of onland tsunami flow depth and runup, both on islands in close proximity to AK (including the August 2019 authors' drone survey), and in the far-field on the coasts of Java and Sumatra.

The combined subaerial and marine data sets, and results presented here, constrain the style and mechanism of the AK lateral collapse and also test current volcanic landslide-tsunami models, which can be used to predict the behavior of similar events at other volcanic islands. The results, therefore, are an important contribution towards improved assessment of tsunami hazard from

analogous events in the future, and also provide an improved basis for developing mitigation strategies for volcanic tsunamis.

2 Background and earlier modeling work

2.1. Geologic and volcanologic context

AK (Fig. 1) is a composite volcanic cone that developed on the northeast margin of the 250 m deep flooded caldera formed by the 1883 eruption of Krakatau (Figs. 2a,3a; Camus et al., 1987; Stehn, 1929). It developed from and so is aligned with the feeder vents of the 1883 Krakatau eruption (Verbeek, 1885, 1983). During the past 90 years of frequent eruptive activity, AK has grown from a submarine volcano to a subaerial edifice, emerging in 1929. With a pre-2018 collapse height estimated at about 335 m (Grilli et al., 2019), it formed an island with a diameter of 1.5-2 km. On the SW flank of AK, coastline retreats of several hundred meters in 1934, 1935 and 1949 (Neumann van Padang, 1983; Hunt et al., 2021) imply long-lived instability of the edifice on this sector (Hunt et al., 2021). The NW-SE orientation of the retreats align with both the underlying caldera-wall scarp and the 2018 collapse scar (Fig. 2a). The retreats are a result of two related factors: i) AK's location on the NE margin of the 250-m deep 1883 caldera; and ii) the asymmetrical pattern of island growth (see discussion in Hunt et al., 2021). The early submarine activity of AK before and during first emergence of the island in 1929 was dominated by phreatomagmatic explosions (Umbgrove 1928; Stehn 1929). Similar explosions continued after first emergence and built-up a low-angle tuff cone around a vent to which the sea continued to gain access until the 1960s. At that time the vent dried out and further subaerial eruptive activity produced lava flows on the SW side of the island, and Vulcanian and Strombolian explosions that built up a scoria cone around the vent (Siswowidjoyo, 1983). This activity continued into the 21st

166 Century, with numerous small eruptions punctuated by more violent explosive episodes, giving
167 the island its pre-collapse form of steep-sided central pyroclastic cone, with lava deltas extending
168 the island on most sides, except the sheltered NE where the tuff cone rim was at its highest, but
169 especially in the NW and SE (Abdurrachman et al., 2018). During a subaerial eruption in 1981
170 (Camus et al., 1987), a ~2 m high tsunami was recorded on Rakata, a remnant of the 1883 eruption
171 and the southernmost and largest island of the contemporary Krakatau archipelago (Fig. 1), which
172 was inferred to originate from a small flank landslide. The event highlighted the potential
173 instability of the southwest flank of the volcano (Camus et al., 1987) but, apart from this, no other
174 tsunamis from AK have been reported.
175 The recent period of AK volcanic activity started in June 2018 and continued into
176 December (https://volcano.si.edu/volcano.cfm?vn=262000), producing Strombolian explosions,
177 lava flows, and ash plumes reaching altitudes of up to 5 km (Anon, 2018; Fig. 2 in Paris et al.,
178 2020a; Figs. S1c,d; Hunt et al.'s 2021 supplementary material). On Dec. 22, 2018, a major lateral
179 collapse occurred on AK's southwest flank which discharged volcaniclastic material into the sea
180 and triggered a destructive tsunami (Andersen, 2018; PVMBG, 2018). Based on seismic records
181 (Gurney, 2018), eyewitness reports (e.g., Andersen, 2018; Perttu et al., 2020), and the agreement
182 of modelled waves with tsunami arrival times at tide gauges (Ina-COAP, 2019; see below; Fig. 1a,
183 Table 3), Grilli et al. (2019) estimated that the collapse took place at 20:55′–57′ (UTC + 7), a time
184 range later confirmed and used by other authors of numerical models (e.g., Borrero et al., 2020;
185 Mulia et al., 2020; Paris et al., 2020a; Zengaffinen et al., 2010), and confirmed in the interpretation
186 of seismic signals by Walter et al. (2019), who timed the collapse at 20:55′. Within 30 minutes of
187 the collapse a tsunami flooded the coasts of west Java and southeast Sumatra, causing up to 13.5
188 m on-land runups. The tsunami struck near high tide (+1.5 m above the vertical datum on average

189 at four tide gauge in Java and Sumatra; Fig. 1a), which increased its impact (AHA, 2018; Muhari,
190 2018, 2019; Grilli et al., 2019; TDMRC, 2019).
191
192 *2.2. Previous modeling of the 2018 AK event*
193 In light of the modelling published by Giachetti et al. (2012), Grilli et al. (2019) performed
194 the first comprehensive numerical simulations of the Dec. 22nd 2018 AK collapse, based on
195 satellite observations on the days following the event, drone and field surveys of near-field tsunami
196 impact conducted in early January 2019 (Reynolds, 2019; TDMRC, 2019; Fig. S1), and historical
197 data on the growth of AK (see, e.g., Hunt et al., 2021). The modelling of AK's flank collapse and
198 tsunami generation was based on a range of failure surfaces with corresponding collapse volumes
199 of 0.22-0.30 km^3 and used the three-dimensional (3D) non-hydrostatic (NH) model NHWAVE
200 (Ma et al., 2012, 2015; Kirby et al., 2016), in which the collapse was represented by a depth-
201 integrated (hydrostatic) layer of a granular material or dense viscous fluid. From the modelling it
202 was proposed that a 0.27 km^3 collapse volume produced the modelled tsunami that best reproduced
203 the near- and far-field tsunami propagation and impact, with the far-field modeling using the fully
204 nonlinear and dispersive Boussinesq model FUNWAVE (Shi et al., 2012). In these simulations a
205 90 or 100 m Cartesian grid was used in each model, respectively, with 5 vertical layers in the 3D
206 NHWAVE grid.
207 Numerical simulations of the 2018 AK collapse and tsunami post-dating Grilli et al. (2019),
208 detailed in the following paragraphs, were also based on hypothetical source parameters derived
209 from a variety of, mainly indirect, data. In these studies, the various assumed/hypothetical failure
210 surfaces gave collapse volumes in the range ≈ 0.14-0.33 km^3, which were both smaller and larger
211 than the 0.27 km^3 of Grilli et al.'s (2019). In Ye et al.'s (2020) study, inversion of broadband

212 seismic data was used to infer a collapse volume of ≈ 0.20 km^3. In some studies, an empirical
213 analytical or experimental (from laboratory tests) landslide source was specified directly on the
214 free surface without an actual modeling of the source (e.g., Heidarzadeh et al., 2020a; Borrero et
215 al., 2020). In other modeling studies, new interpretations of subaerial observations were used (see
216 Hunt et al., 2021 for a discussion) and the flank collapse and tsunami generation modeled for a
217 variety of volumes and geometries (e.g., Mulia et al., 2020; Ren et al., 2020; Omira and Ramalho,
218 2020; Paris et al., 2020a; Zengaffinen et al., 2020; Dogan et al., 2021). In the latter models, tsunami
219 generation was based on various rheologies (granular, viscoplastic, Bingham) and simulated using
220 a two-dimensional (2D) two-layer model. There were also important differences in tsunami
221 propagation models used in these various studies, with some using a dispersive model (e.g., Mulia
222 et al., 2020; Paris et al., 2020a; Borrero et al., 2020) and others using a non-dispersive tsunami
223 propagation model (e.g., Heidarzadeh et al., 2020a; Ren et al., 2020; Omira and Ramalho, 2020;
224 Dogan et al., 2021). As landslide tsunamis are typically made of shorter, more dispersive, wave
225 trains, they often require the use of a dispersive long wave model for their accurate modeling (e.g.,
226 Ma et al., 2012; Glimsdal et al., 2013; Tappin et al., 2014; Grilli et al. 2015, 2017; Schambach et
227 al., 2019). For the 2018 AK event, Paris et al. (2020a) concluded that dispersive effects were
228 important during tsunami generation and propagation, whereas Zengaffinen et al. (2020) found
229 that they were not large in the shallow water areas of the Sunda Straits (as would have been
230 expected), to the north and south of AK. More specifically:

231 • In one of the more comprehensive recent studies, Zengaffinen et al. (2020) modeled the
232 tsunami using the rate of mass release, the landslide volume, the material yield strength, and
233 orientation of the landslide failure plane, together with the 2D two-layer depth-averaged
234 coupled model BingClaw, to identify different failure mechanisms, landslide evolution, and

tsunami generation. The depth-integrated landslide layer was based on a viscoplastic flow rheology, coupled with depth-averaged long wave and shallow water type models to simulate tsunami propagation. With a volume of 0.28 km^3, identical to that of Giachetti et al. (2012), the numerical simulations provided a reasonable match to the observed tsunami surface elevation amplitudes and inundation heights in the far-field. Overall the results were consistent with those of Grilli et al.'s (2019) preferred 0.27 km^3 scenario, and discrepancies between the simulated and observed arrival times at the offshore gauges were attributed to the (poor) accuracy of the available bathymetry, rather than to their model. To match these, to the north of Krakatau, Zengaffinen et al. (2020) arbitrarily increased the water depths in this area.

- Paris et al. (2020a) used the 2D two-layer depth-averaged coupled model AVALANCHE, which features a granular rheology and a Coulomb friction for the slide description, with dispersive effects for the water flow part. From pre- and post-collapse satellite and aerial images, and a satisfactory comparison of the simulated water waves with far-field observations (tide gauges and field surveys), they reconstructed a total (subaerial and submarine) landslide volume of 0.15 km^3, at the lower end of the volume range in the various studies described here.
- Ren et al. (2020) applied a 2D two-layer depth-averaged coupled non-dispersive model throughout, with the slide layer modeled as a dense fluid. Using two nested grids, the smaller having a 30 m resolution and the larger a coarse 230 m resolution, and 0.1-0.3 km^3 collapse scenarios, they showed a reasonable agreement with the first wave at the far-field tide gauges.
- Mulia et al. (2020) integrated the landslide thickness over the estimated source area and, assuming a failure surface similar to that of Giachetti et al. (2012), except for a slightly steeper slope, obtained a collapse volume of 0.24 km^3 (slightly smaller than that of Giachetti et al., 2012, and Grilli et al., 2019). Using the 2D two-layer depth-averaged coupled model VolcFlow

to simulate avalanche dynamics (here assuming a constant retarding stress throughout), and FUNWAVE for the far-field tsunami, their landslide generated higher than 40 m waves in the vicinity of the volcano. As with other studies the tsunami attenuated rapidly as it propagated away from the generation area, resulting in lower than 2 m wave heights at tide gauges around the Sunda Strait.

- Omira and Ramalho (2020) used a multi-layer viscoplastic model to simulate the collapse, with a 2D slide layer based on a Bingham rheology and an upper water layer in which the (non-dispersive) Nonlinear Shallow Water Equations are solved. They simulated a sequence of two failures (5 s apart) of 0.1 and 0.035 km^3, respectively, and computed both the near- and far-field tsunami propagation using the same model. They used high-resolution bathy/topo data (see Table 1) to create a 10 m DEM, but it is unclear what their model resolution was. The collapse generated a 45 m leading wave near the volcano, which caused up to 60 m runup on nearby islands. Although they obtain a reasonable agreement at the 4 tide gauges for the leading wave, they indicate strong tsunami dissipation in the far-field, only computing maximum runups of 4 m in Java. This could result from their non-dispersive model and/or excessive numerical dissipation and use of a coarse grid in the simulations.
- Finally, in the latest study to date, Dogan et al. (2021) modeled a 0.25 km^3 collapse (based on a maximum elevation for AK of only 260 m, smaller than used in other studies) and its tsunami generation, using Imamura and Imteaz (1995)'s two-layer long wave model. Tsunami propagation to the far-field was then simulated using the non-dispersive NSW model NAMI DANCE, in an 80 m resolution grid. Little details are given of the parameterization of their dense fluid rheology in the slide model or the rationale for defining the pre- and post-failure volcano geometry, including the selected failure surface. However, they show a good

agreement with both arrival times and elevation time series measured at the 4 tide gages in Java and Sumatra. Based on observed bathymetric changes in pre- and post-event surveys, they model tsunami generation from additional submarine slope failures on the north and south sides of the caldera, but conclude that these did not contribute to and hence were not simultaneous with AK's 2018 event.

The main characteristics of the previous modeling studies discussed above are listed in Table 1.

All of these studies used different AK collapse scenarios and a wide spectrum of approaches and tsunami modelling, but the differences in tsunami elevations predicted at the far-field tide gages were small; there were larger differences in predicted far-field runups, but some of these could be explained by differences in grid resolution and model physics. While details of a tsunami source become less important when the distance from the source increases, here, the small differences in the predicted far-field tsunami impact between various modeling studies were in great part because the landslide mechanisms were based on inverse methodologies and, hence, were partly or wholly hypothetical. So, although the recorded far-field tsunami was reproduced, it was not based on the actual collapse mechanism but, at best, on direct evidence such as from satellite imagery, or indirect evidence such as from seismic observations of the subaerial collapse. In all studies, hydroacoustic data such as multibeam bathymetry or seismic reflection data, to confirm the submarine components of the landslide source mechanism, was lacking. In the modelling studies using a semi-empirical landslide source (e.g., Borrero et al., 2020; Heidarzadeh et al., 2020a), the collapse volume and hence source strength were adjusted based on field observations of the tsunami (e.g., near- and/or far-field runup and tide gauges). The validation was then from the forward numerical modeling of the tsunami, which is rather circular. Other modeling

303 studies using an actual slide mechanism also adjusted or confirmed their collapse scenario and
304 volume, to achieve a good agreement of tsunami simulations with far-field data.

305 While making some source adjustments to best match the far-field tsunami observations,
306 most previous studies also demonstrated a moderate sensitivity of the predicted far-field tsunami
307 impact to the landslide source characteristics. This shows that far-field tsunami observations alone
308 cannot fully constrain the 2018 AK collapse parameters and, hence, stresses the need for also using
309 near-field tsunami data and, more importantly, marine surveys to do so, as will be done in this
310 work.

311

312 **3 Methods**

313 3.1 *Study area, computational grids, and bathymetric/topographic data*

314 Figure 1a shows the entire study area and the footprint of the two computational grids used in the
315 simulations of: (grid G2) AK's collapse and tsunami generation/near-field impact, using the 3D
316 model NHWAVE; and (grid G1) tsunami propagation and far-field impact, using the 2D model
317 FUNWAVE, together with their bathymetric and topographic data.

318 The near-field Grid G2 is defined with a $\Delta x = \Delta y = 30$ m horizontal resolution (Table 2),
319 from the composite bathymetry developed by Hunt et al. (2021), based on the new multibeam
320 echosounding (MBES) bathymetry acquired during their August 2019 field surveys (Figs. 2a,b),
321 combined with: (i) unpublished Sparker seismic reflection profiles acquired in 2017; (ii) basin
322 bathymetry from Deplus et al. (1995) manually modified within the deep part of the caldera to add
323 up to 10 m of sediment infill between 1995 and 2018 (based on interpreted seismic profiles in Hunt
324 et al., 2021); (iii) an 8 m DEM for the islands of the Krakatau archipelago (from

325 http://tides.big.go.id/DEMNAS); and (iv) topography from Gouhier and Paris (2018) for AK itself,
326 based on the DEMNAS DEM, with modifications to account for island growth in 2018.

327 The far-field grid G1 (Fig. 1a; Table 2) is Cartesian with a 50 m resolution and its
328 bathymetric and topographic data is interpolated from Giachetti et al. (2012)'s 100 m resolution
329 dataset, which was developed outside of Krakatau's caldera based on GEBCO data. The GEBCO
330 data is referred to mean sea level (MSL); GEBCO, however, indicates that in some shallow water
331 areas, their dataset includes data from sources having a vertical datum other than MSL. Note that
332 even though the bathymetric data is coarser than the model grid, using a finer model grid allows
333 for a more accurate resolution of the nearshore wave physics. Our model grid is also finer than the
334 90 m resolution used by Grilli et al. (2019).

335 Regarding the reference mean water level (MWL), Grilli et al. (2019) indicated that, when
336 the tsunami was generated, the average elevation at the four tide gauges (WG 6-9; Fig. 1a; Table
337 3) was approximately +1.5 m over the vertical datum. Because of this, simulations were based on
338 adding 1.5 m to the bathymetric data (i.e.using water depths of MWL = MSL + 1.5 m, where it is
339 assumed that the bathymetric datum is mean sea level (MSL). However, as noted above, there may
340 be inconsistency in the vertical datum used in the bathymetric compilation. Moreover, both at the
341 time and still at present, the reference datum for the tide gauges is unknown, but in the absence of
342 other constraints we assumed a common vertical datum for our bathymetric datasets and the tide
343 gauges. Given the local tidal range, the elevation at the time of the tsunami was more likely
344 between 0.5 and 1.0 m above the true MSL (see discussion in the Supplementary file #S3). To
345 assess the effect of the uncertainty in both nearshore bathymetry and in the tide gauge datum value
346 with respect to the MSL, we performed a sensitivity study of model results to the assumed MWL
347 (for the likeliest collapse scenario defined in the next section; see Supplementary file #S3 and

348 Table 5). This demonstrates that, within the range MSL +0.5 to + 2 m, model results were little
349 affected by the water-depth adjustment, with each of the MWL values giving results that compared
350 similarly well to the field data. Hence, for consistency and comparison with our earlier modeling
351 work (Grilli et al., 2019), we selected the same MWL = MSL + 1.5 m in this study.. This value
352 was added to the interpolated bathymetric data for both Grid G1 and G2, prior to performing
353 tsunami simulations. When comparing simulation results to field data referenced to MSL or some
354 other datum, a relevant correction was made to the field data.

355 3.2 *Landslide source model*

356 The landslide source model was defined on the pre-collapse bathymetry/topography grid G2
357 defined above, using constraints that drew on the post-collapse bathymetric survey of Hunt et al.
358 (2021), particularly to define the boundaries of the submarine failure surface, as well as an updated
359 interpretation of the subaerial failure plane. The latter was based on a sequence of Synthetic-
360 Aperture Radar (SAR) satellite images collected in the days following the collapse, alongside
361 aerial imagery collected on Dec. 23rd 2018. These images proved particularly important in defining
362 the northern and southern bounds of the subaerial collapse scar, since their position could be
363 precisely defined based on the complex coastal shape of the lava deltas. The COSMO-SkyMed
364 SAR imagery from Dec. 23rd 2018 confirms the shape of the failure scar between these two coastal
365 points (cf. Hunt et al., 2021) and was used to pick both the upper line of the headwall and the point
366 where this intersected sea-level (i.e. the 0-m contour; e.g., Figs. 2c,d). These two boundaries were
367 used to define the subaerial dimensions of the modeled landslide failure plane, and we thus
368 consider this component of the failure surface to be fixed in the range of source models described
369 below.

To address the limitations of the published tsunami source models of the collapse mechanism and the landslide resulting from the 2018 AK flank collapse, as mentioned before, MBES bathymetry and seismic data were acquired in the 250 m deep basin on the southwest flank of the volcano in August 2019 (Hunt et al., 2021). From detailed analyses of this marine survey data (Figs. 2a,b) these authors mapped the submarine landslide resulting from the volcanic collapse and estimated the landslide outrun deposit volume at 0.214 ± 0.036 km^3. Rather than being extensively disintegrated, the submarine deposit is mainly composed of large intact blocks (Figs. 2a,b), confirming that the event occurred as a single *en masse* slide with limited fragmentation, rather than in a more piecemeal, multi-staged process. This mechanism is also confirmed by seismic data (Gurney, 2018). From these characteristics, while there were many large landslide blocks in the deposits (up to hundreds of meters across), a granular slide rheology was deemed more relevant in our subsequent modeling than a dense fluid rheology, which is more appropriate for debris flows (although both were simulated for completeness). An additional unit, to the southwest of this main deposit, with a volume of 0.022 ± 0.006 km^3, was interpreted as a secondary sediment failure (i.e., debris flow), resulting from sediment mobilized by the primary landslide emplacement and seafloor incision (Hunt et al., 2021).

A range of volumes were defined for the 2018 AK collapse, based on the marine survey in combination with new analyses of subaerial observations from high-resolution satellite imagery, and aerial photography. This estimated a subaerial collapse volume of 0.098 ± 0.019 km^3 (cf. Hunt et al., 2021). Beneath sea level, the lateral margins of the collapse scar were defined using bathymetric features on the submerged flank of AK, evident on the post-collapse marine survey. A subtle step in the submerged SW flank, at -100 to -120 m described by Hunt et al. (2021), that may correspond to the base of the failure plane, was used to define the minimum collapse volume

393 scenario (Figs. 2c,d), which has a shallower failure surface than that of Grilli et al. (2019) for their
394 minimum 0.22 km^3 volume scenario. Using the features identified by Hunt et al. (2021), the
395 boundary of the submarine failure plane was estimated as a broadly elliptical form, and this
396 boundary was then projected onto our pre-collapse bathymetric grid. This was used to define a
397 smooth concave failure plane, constrained by the gradient of the subaerial scar and the requirement
398 to cut the vent position beneath sea-level, defining a minimum collapse volume of 0.175 km^3.
399 Precise identification of the shape and margins of the failure surface is still uncertain because of
400 burial by post-collapse deposits. Additional features on the NW and S flank of AK, that align with
401 the subaerial margins of the scar, alongside deeper features on the SW flank (cf. Hunt et al., 2021),
402 may also relate to the collapse plane and were used by Hunt et al. (2021) to define a possible larger,
403 deeper-seated failure surface. Using the same approach as described above, the failure volume in
404 this largest possible scenario was estimated at 0.313 km^3 (Figs. 2c,d). Both end-point collapse
405 volumes include the 0.098 km^3 subaerial component.

406 Comparing the deposit volume, estimated purely from the MBES and seismic reflection
407 survey, to the failure volumes estimated based on the inferred failure surface and geometry, we
408 find good consistency. The main part of the landslide deposits form a blocky mass, identified in
409 the August 2019 MBES data (modeled a,b) and interpreted as representing material directly derived
410 from the island flanks, with a volume of 0.214 ± 0.036 km^3. The estimated primary deposit volume
411 of 0.214 km^3 lies between the two end-point failure-surface-derived volumes described above
412 (Figs. 2c,d). Given that the failed mass is likely to have expanded upon fragmentation, and is
413 potentially bulked via seafloor erosion, an increase in the volume of the landslide deposit,
414 compared to the volume derived from the shallowest estimated failure surface, could potentially
415 be accounted for by these phenomena. A further uncertainty arises from the possibility that some

of the failed mass could have remained within the scar region and been subsequently buried (although there is no evidence to suggest that this volume is significant), and would not be included in the estimate of deposit volume derived from marine geophysical data. Consequently, although quite unlikely, we cannot entirely reject a scenario with a deeper-seated failure plane and a larger source volume, up to a maximum of 0.313 km^3, although our interpretation is that the primary failure volume was likely closer to our minimum estimate (0.175 km^3).

Within the blocky landslide deposit (Figs. 2a,b), it can be assumed that transport of all material derived from the volcano flanks was tsunamigenic. There is potential for expansion and incorporation of seafloor material during slide motion, and we thus use the scar-derived volumes rather than the deposit volume to define the range of source-volumes for tsunami modelling. In addition to this, mobilization of seafloor sediment triggered by primary landslide emplacement (forming the secondary debris flow deposit) may also have contributed to tsunami generation. However, given that this must have followed the main stage of landslide motion, was in relatively deeper water, and was an order of magnitude smaller in volume, we assume that this material was not significant in contributing to the main tsunami generation. The 0.022 ± 0.006 km^3 debris flow volume also falls well within the range of uncertainties of the estimated landslide volume.

In the modeling, the above uncertainty in AK's collapse parameters is represented by defining four landslide (and failure surface) geometries and corresponding volume scenarios, for which we use the same subaerial pre-collapse geometry in every case (based on the SAR-derived collapse-scar position), intersecting the NE flank at about 100 m elevation (Fig. 2d). For the submarine surface, we use the minimum and maximum bounds of the failure surface described by Hunt et al. (2021) and discussed above, projecting the positions of the defined collapse margins onto our pre-collapse model grid. Alongside this, we define two intermediate scenarios. The four

scenarios have a maximum depth on the SW flank ranging from -80 to -220 m (Fig. 2d) and their failure surfaces all cut the active vent position at depths ranging from 25 to 40 m, which is consistent with the vigorous Surtseyan eruptive activity that immediately followed the collapse (Hunt et al., 2021). Using the pre-collapse AK topography (maximum 335 m), refined based on high-resolution satellite images (Novellino et al., 2020) and the assumed concave failure surfaces, the volumes associated with the four scenarios were computed to: (1) 0.313; (2) 0.272; (3) 0.224; and (4) 0.175 km^3. The latter two compare closely with the deposit volume estimate, given uncertainties and allowing for some degree of expansion and/or bulking by erosion, while the first two scenarios are larger, but consistent with some bathymetric features and the possibility that some of the failure mass remained within the collapse scar. The first scenario is close to the largest volume originally simulated by Grilli et al. (2019), and the second is close to what they concluded to be the likeliest scenario.

Among these scenarios, the third one, with a 0.224 km^3 volume, is deemed the likeliest volume scenario in the modeling, in terms of providing the best representation of the tsunamigenic mass movement consistent with the marine geophysical data. Given that there remain uncertainties in the precise form of the failure plane, the mean deposit volume of 0.214 km^3 from Hunt et al. (2021) is the best representation of the tsunamigenic mass (even if we cannot constrain the extent of expansion and bulking) and, the 0.224 km^3 volume also allows for the possibility of some tsunamigenic contribution from the associated secondary debris flow. The post-collapse bathymetry for the likeliest scenario (0.224 km^3) is shown in Figs. 1c and 3b. Note that the latter figure shows that, as expected, the specified failure surfaces are not planar but slightly concave. This is a necessary shape given the relatively steep gradient (30-40 degrees) of the subaerial failure plane (constrained from SAR imagery and consistent with the volcanic vent being cut beneath sea-

462 level) but the need for the foot of the failure to emerge within the submerged flank of AK, and is
463 also a failure-surface shape typical of the morphology of volcanic lateral collapses.

464

465 3.3 *Tsunami generation and propagation simulations*

466 3.3.1 *Numerical tsunami models.*

467 Two numerical models are used in simulations of AK's 2018 collapse and tsunami
468 generation, propagation and coastal impact, which are briefly described below.

469 NHWAVE (Ma et al., 2012), a three-dimensional (3D) non-hydrostatic model, is used to
470 simulate both AK's volcanic collapse scenarios, and the corresponding tsunami generation and
471 near-field impact, on AK and surrounding caldera islands, in Grid G2 with a 30 m horizontal
472 Cartesian grid with 1,155 by 9,55 cells, using 7 boundary fitted water layers in a vertical σ-
473 coordinate system (Figs. 1b,c; Table 2). With one layer, the model provides the same order of
474 dispersion as a Boussinesq model such as FUNWAVE, detailed hereafter, and higher-order
475 dispersion effects when using more layers. NHWAVE has been used, and experimentally validated
476 (e.g., Ma et al., 2012), to model tsunami generation from solid slides (landslides or slumps) (e.g.,
477 Grilli et al., 2015; Schambach et al., 2019) and from dual sources coseismic/solid submarine mass
478 failures (Tappin et al., 2014). NHWAVE was extended to simulate tsunami generation by
479 deforming slides, both submarine and subaerial, assumed to behave as either a granular medium
480 or a dense Newtonian fluid (Ma et al., 2015; Kirby et al., 2016). These NHWAVE models were
481 applied to case studies for deforming slide sources (e.g., Grilli et al., 2017b, 2019; Schambach et
482 al., 2019), and validated based on laboratory experiments for those studies (Grilli et al., 2017b), as
483 well as for dual sources involving a combination of coseismic and deforming underwater/subaerial
484 slides (e.g., Grilli et al., 2019; Schambach et al., 2020a,b).

485 Since the work of Grilli et al. (2019), a new version of NHWAVE has been developed
486 (Zhang et al., 2021a,b) that includes effects of vertical acceleration (i.e., non-hydrostatic pressures)
487 within the slide material layer, which was neglected in the earlier implementation (Ma et al., 2015).
488 Considering the steep slopes of both AK and the surrounding islands, it was anticipated that such
489 effects might be important. This was confirmed here by comparing, in Supplementary file #2,
490 simulations of the Grilli et al. (2019) preferred volume scenario (0.272 km^3), with both granular
491 and viscous rheologies, and with and without the non-hydrostatic effects included in the equations
492 for the slide layers. Results for both rheologies showed that slide motion and wave generation are
493 significantly affected, with larger waves generated and much larger runups occurring on the near-
494 field islands, particularly Panjang and Sertung, when non-hydrostatic effects are neglected. When
495 comparing with near-field runup measured in field surveys, a much better agreement was obtained
496 with the newer version of the model that accounts for non-hydrostatic effects within the slide layer.
497 For these reasons, this newer version of NHWAVE by Zhang et al. (2021a,b) was used in the
498 present study.
499 FUNWAVE-TVD (Shi et al., 2012; version 3.0 is used), a two-dimensional (2D) fully
500 nonlinear Boussinesq wave model, is used to simulate far-field tsunami propagation and coastal
501 impact in Cartesian Grid G1 with a 50 m resolution and 3,900 by 3,680 cells (Fig. 1a; Table 2); a
502 Cartesian rather than a spherical grid is acceptable in view of the small geographic area considered
503 here. To improve dispersive properties, the horizontal velocity used in this Boussinesq model is
504 that at a depth z = -0.531 h. To prevent reflections from the open boundaries of grid G1 (Fig. 1a),
505 10.8 km (or 216 grid cells) wide sponge layers are specified along its 4 boundaries.
506 Both NHWAVE and FUNWAVE-TVD used a Courant number and Froude cap condition
507 to adaptively specify the time step in simulations to achieve optimal accuracy. In shallow water

508 and during runup this can lead to using prohibitively small time steps, which is prevented here by
509 specifying a minimum depth truncation of 1 m and 0.05 m in the NHWAVE and FUNWAVE
510 simulations, respectively. The 0.05 m minimum depth has little effect on FUNWAVE simulations
511 of the far-field tsunami impact. In the near-field, considering the very large waves and runups
512 modeled with NHWAVE, the 1 m minimum depth also does not significantly affect simulation
513 results. Both models are parallelized with MPI, allowing efficient implementation on large
514 computer clusters. Here we typically used 20 processors to run each scenario. Finally, both models
515 are open source and available on *github*, together with their user manual and benchmarking
516 examples.

517 3.3.2 *Modeling methodology.*

518 Simulations of AK's collapse and tsunami generation and near-field impact are first performed in
519 grid G2 with NHWAVE, for the 4 volume scenarios, and for each of those, assuming either a
520 granular or a dense fluid rheology (Table 4). When the slide is fully at rest and waves approach
521 the boundary of grid G1 (Fig. 1a), NHWAVE results for surface elevation and horizontal velocity
522 interpolated at 0.531 times the local depth are used to initialize FUNWAVE simulations in Grid
523 G1. These are then run for another 2 hours of tsunami propagation time, to make sure all the
524 diffraction, and multiple reflection effects on the tsunami from the shores and many islands of the
525 Sunda Straits are included in the results.

526 In NHWAVE simulations, for each of the four specified collapse surfaces and volumes
527 (Figs. 2c,d), we use the same parameterization of the slide rheology as in Grilli et al. (2019), i.e.:
528 (i) a Newtonian fluid of density ρ_c = 1,550 kg/m^3 and the kinematic viscosity of a debris flow, ν_c
529 = 0.5 m^2/s; or (ii) a granular medium with ρ_c = 1,900 kg/m^3 for the solid part and, similar to
530 Giachetti et al. (2012), an internal friction angle ϕ_{ic} = 10°, a basal friction angle ϕ_{bc} = 2°, and a 40%

porosity. With this data, assuming a water density ρ_w = 1,025 kg/m^3, the average density of the granular medium is ρ_{ac} = 1,550 kg/m^3 (Table 5). For each of these 8 scenarios, NHWAVE was run up to 420 s; however, results showed that the time when the generated tsunami waves approach the boundary of grid G1 is t = 380 s (e.g., Fig. 7h), which is used to prevent any perturbation of the solution.

Finally, in both model grids, in the absence of site-specific data we specify a constant bottom friction coefficient C_d = 0.0025, which corresponds to coarse sand. While this value may be too small to model friction on the rough walls of the 250 m deep caldera to the SW of AK, earlier work has shown that bottom friction only significantly affects tsunami propagation (reducing tsunami elevations) over shallow areas where propagation distances represent many dominant wavelengths (Tehranirad et al., 2015). In this case, the bottom velocity caused by the long tsunami waves (in terms of wavelength to depth ratio) is consistently large. Considering the fairly short dominant period of the generated waves, here, bottom friction will only significantly affect tsunami propagation towards Java and Sumatra, in the shallow eastern side of the Sunda Straits. In the caldera to the SW of AK, however, both the water depth is large and the tsunami propagation distances are short, and bottom friction effects are thus expected to be small; hence, the accuracy of the selected C_d value is not important.

3.4 *Tsunami field survey data*

To validate our numerical model results, we used a comprehensive set of data, including marine field surveys, satellite images, bathymetric data as discussed above, and onshore surveys of tsunami impact (Figs. 12-16). The onshore survey data included: (i) the tree line drone survey conducted on Rakata, Sertung and Panjang during our August 2019 field campaign (Figs. 11, 13),

554 and (ii) the runup and flow depth measurements made in the near- and far-field by TDMRC (2019),
555 Muhari et al. (2019), Putra et al. (2020), Borrero et al. (2020), and Heidarzadeh et al. (2020b). In
556 addition, we used the extensive video made by Reynolds (2019), during his 01/11/2019 near-field
557 drone survey of AK and the three surrounding islands, of which salient images were extracted by
558 Grilli et al. (2019) (see their supplementary Fig. S8). One example is in Fig. S1f. These surveys
559 show that, in the near-field, the tsunami generated by AK's 2018 collapse caused up to 85 m runups
560 on the islands of Rakata and Sertung and, in the far-field, up to 13.5 m runups on the nearby coasts
561 of Java and Sumatra.
562 Additionally, as in Grilli et al. (2019) and all other modeling studies, time series of surface
563 elevations simulated for each scenario are compared with detided free surface elevations measured
564 at 4 tide gauges located at (Fig. 1a; Table 3): (5) Serang, Marina Jambu, (6) Ciwandan, (8) Kota-
565 Angung, and (9) Panjang. Grilli et al.'s (2019) Supplementary file #3 explains how the raw data,
566 measured at a 1 minute interval, was detided to obtain the tsunami signal (their Fig. S5) and shows
567 where each tide gauge was located (their Fig. S4), pointing out that each gauge is surrounded by
568 some reflective (or dissipative) coastal structures, not represented in the model grids, that can affect
569 tsunami signal in various ways (including seiching). Table 3 provides the location of each tide
570 gauge, its depth in grid G1 and the arrival time of both a 1 cm tsunami elevation and the first
571 significant wave crest. Fig. 10 shows the complete (detided) tsunami time series measured at each
572 gauge by two different independent instruments operating at each gauge (see details in Grilli et al.,
573 2019); there are some differences (sometimes large) between the measurements of the two
574 instruments at each gauge, which allows quantifying experimental errors. The individual data
575 points in the time series illustrate the coarse 1 minute temporal resolution of the measured signal.
576

4 Tsunami simulation results

4.1 *Slide motion and deposits*

Results of combined NHWAVE-FUNWAVE simulations in Grids G2 and G1 of the 4 volume scenarios ((1) 0.313; (2) 0.272; (3) 0.224; and (4) 0.175 km^3), each with either a granular or viscous rheology (scenarios 1-8 in Table 4), are discussed hereafter.

Figures 4 and 5 show examples of slide motion and free surface elevations simulated with NHWAVE. Fig. 4 first compares results in a vertical plane along a SW transect into AK, for the likeliest volume scenario (0.224 km^3), using either a granular or viscous rheology. We see that the change in rheology only moderately affects slide deformation for small times ($t < 80$ s), and hence corresponding wave generation, but that differences in slide runout are much larger later in time ($t \geq 120$ s), although this stage of motion is no longer tsunamigenic as the slide deposits are too deep. At $t = 200$ s (Fig. 4h) the granular slide deposits have nearly stopped and have mostly accumulated in the caldera, reaching up to a 94 m thickness at the toe of AK's failure surface, whereas the viscous slide deposits have moved further onto the caldera bottom and are still moving. While the granular slide deposits appear to be located in the general area where the actual deposits were mapped during the August 2019 marine survey (Figs. 2b,c) (Hunt et al., 2021), the viscous slide deposits have moved beyond this area; hence simulations based on the granular rheology appear to be more consistent with field data than those with the viscous rheology. This is confirmed in Fig. 5, which shows greater details of the 3D granular slide motion and deposits for the same volume scenario. Here in the last panel at $t = 420$ s (Fig. 5h), we see more clearly where the main slide deposits are located (i.e., their runout) and how thick they are (up to 94 m) at the end of the motion, which is consistent with observations of slide deposits from the marine geophysical survey (Hunt et al., 2021) (compare Fig. 5h with Fig. 2a). In view of the modeled slide idealization by a

600 continuous granular medium, our results for both the slide deposit location and thickness appear
601 to be quite reasonable. It should be noted that while the main collapse deposits are to the SW, the
602 simulation produces a layer of a few meters of granular material deposited on the opposite, NE
603 side of AK and to the NW and SE, which caused small additional wave generation in those
604 directions that however did not affect far-field results which was dominated by larger waves caused
605 by the main collapse. Given the low degrees of fragmentation evident from the very large blocks
606 in the observed deposit (Fig. 2b), these features in model results may not be representative of an
607 actual deposit distribution and are more likely an artifact of a landslide model based on a
608 continuous granular rheology. A similar discrepancy between observed and modeled deposits was
609 noted by Ward and Day (2006) in their study of the 1980 Mount St Helens event, which caused a
610 large debris avalanche.
611 Videos of computed slide motions with and without surface elevation, and for a granular
612 material or a viscous slide are given in supplementary material for the likeliest volume scenario
613 (0.224 km^3); see, AK_slide3D_gran.mp4, AK_ slide3D_visc.mp4, AK_wave_slide3D_gran.mp4,
614 AK_wave_slide3D_visc.mp4.
615
616 4.2 *Near-field tsunami generation*
617 Figures 4 and 7 show snapshots of free surface elevation at times t = 10, 20, 40, 80, 120,
618 160, 200, and 380 s, computed for the likeliest volume scenario and a granular or viscous rheology,
619 and Fig. 6 compares time series of surface elevation computed at the 5 numerical wave gauges
620 (Fig. 1b; Table 3) specified in grid G2, for the 8 modeled scenarios (4 volumes and 2 rheologies,
621 scenarios 1-8 in Table 4). Other snapshots of surface elevations for scenarios not shown here look

622 qualitatively similar to those in Fig. 7. Videos of computed surface elevations are given in the
623 supplementary materials.

624 Results in Figs. 4 and 7 show that, in the first 20 s of AK's collapse, a large-scale subaerial
625 slide motion occurs down the volcano, triggering a 50+ m horseshoe-shaped leading elevation
626 wave. From 20-80 s, as the slide moves mostly underwater (for all 4 volume scenarios), an up to
627 30+ m trough (negative elevation wave) forms near the volcano on the SW side, while the leading
628 elevation wave radiates as a cylindrical crest of decreasing height. Figure 6a shows that these
629 processes are well captured at WG 1, which is located directly SW of AK (Fig. 1b; Table 3); at
630 this site, depending on the scenario, a 25-33 m leading elevation wave arrives at $t \approx 60$ s, followed
631 by a 0-10 m trough. At WG 2 and 3, further NW and SW of the volcano, Figs. 6b,c show that, later
632 in time ($t \approx 175$ s), the large elevation wave and its trough (first depression wave) have essentially
633 propagated radially, with only a small decrease in the crest height. The propagation of the
634 horseshoe-shaped leading elevation and first depression waves, with their gradual directional
635 spreading and reduction in elevation, are clearly seen in Figs. 7c to 7h. As these waves propagate
636 away from AK, however, for $t > 80$ s (Fig. 7d), they start interacting with and running up both the
637 N shore of Rakata and S shore of Sertung, causing very large runups.

638 To the NE of AK, for $t > 100$ s, we see a significant tsunami impact occurring on Panjang's
639 southern tip (25+ m runup) and, for $t > 150$ s, a more moderate impact on its northern tip, that are
640 due to both the propagation and refraction around AK's bathymetry of the leading horseshoe-
641 shaped wave (Figs. 7d-f) and later on its reflection off Rakata and Sertung. Finally, in Figs. 7g,h,
642 we see that large waves are propagating in the SW, E and N directions away from AK. For the
643 latter two directions, these waves are well captured at WG 4 and 5 (Figs. 6d,e), where we see

644 leading elevation waves of about 4 and 5 m, respectively. Fig. 7h also confirms that at 380 s, the
645 leading waves have not yet reached and interacted with the outer boundary of Grid G2.

646 Considering the 8 different scenarios, results at WG 1 to 5 in Fig. 6 show that while, overall,
647 all generated waves exhibit the same large-scale characteristics, both a change in collapse volume
648 and rheology affect wave elevation and phase to various extents. Between rheologies, the granular
649 rheology generates slightly smaller leading waves in all cases than the viscous rheology
650 (particularly to the SW), and the larger the collapse volume the larger the wave elevations. [Note
651 that the first conclusion is opposite to that of Grilli et al. (2019) who found that larger waves were
652 generated by a granular slide; this could result from the use here of a much higher grid resolution
653 and the new non-hydrostatic slide model.] At all wave gauges (WG 1-5), the larger leading wave
654 is followed by smaller waves of period as low as T = 30-50 s. Over the 250 m deep caldera, these
655 waves are fully or significantly dispersive. Waves in this period range would be dispersive for
656 depths $h < gT^2/400$ = 3.5-9.8 m, hence for most of their propagation to shore, which justifies using
657 a dispersive long wave model such as FUNWAVE to model AK's collapse far-field tsunami
658 propagation.

659 Fig. 8 shows the envelope of maximum surface elevation computed with NHWAVE in
660 Grid G2 for the likeliest volume scenario (0.224 km^3) and a granular rheology; envelopes for the
661 other scenarios look qualitatively similar and are not shown for the sake of brevity. The figure
662 confirms the large wave generation SW of AK, and shows that large 50-100+ m runups occur on
663 the exposed shores of Rakata and Sertung, and 25 m runup on the south shores of Panjang. These
664 results will be detailed later and compared to field measurements.

665

666 4.3 *Far-field wave propagation and coastal impact on Java and Sumatra*

For each of the 8 scenarios, FUNWAVE simulations were initialized with results of NHWAVE in Grid G2 at 380 s (Fig. 7h), interpolated onto Grid G1, and tsunami propagation and coastal impact were simulated up to t = 7,580 s from the start of the event. Figures 9a-c show snapshots of surface elevation computed with FUNWAVE for the likeliest volume scenario (0.224 km^3) and granular rheology at t = 380, 1800 and 3600 s. Results for the other scenarios are qualitatively similar. After 30 minutes, Fig. 9b shows that leading tsunami waves have started impacting the SW coast of Java, around the Kolijaah and Panaitan Island areas (Fig. 1a), are impacting the south facing coast of Sebesi (Fig. 1a), and are about to impact the coastlines at Ujung Kulon and Serang, Marina Jambu (tide gauge (WG) 5; Fig. 1a and Table 3). To the north of the grid, leading waves are also impacting the SE tip of Sumatra; waves are also propagating in the direction of tide gauges (WG) 6-9 (Fig. 1a; Table 3). After 1 hour of tsunami propagation, Fig. 9c shows a complex pattern of waves in the Sunda Straits, as a result of diffraction-refraction around islands and reflection off the coasts, which justifies performing simulations for a long enough time to capture maximum runup at all locations within Grid G1.

Fig. 9d shows the envelope of maximum surface elevation computed with FUNWAVE in Grid G1, after 7,580 s of simulations, for the likeliest (granular) scenario. AK's collapse generated initial waves with a strong SW directionality and a secondary E and N directionality (Fig. 7h), which translates upon far-field propagation into a maximum impact on the SW coast Java and a relatively smaller impact eastward and northward on the coasts of Java and southern Sumatra (see also Fig. 9b). Additionally, wave propagation is affected by a significant bathymetric feature, the moderately steep S-N oriented (around Lon. E. 105.3) linear scarp that divides the shallow eastern half of Sunda Straits from the much deeper Semangka Trough to the west (Fig. 1a). As can be seen in Fig. 9b (and in the animation of model results provided in supplementary material), this

690 bathymetric feature causes a wave guiding effect that reinforces waves to the south onto Panaitan
691 Island, where some of the largest flow depths and runups were measured, and also guides some
692 waves to propagate northward. Comparing bathymetric contours with the maximum envelope in
693 Fig. 9d, we see that little tsunami energy propagated west of Lon. E. 105.3, and that bathymetric
694 focusing also occurs towards Ujung Kulon (Fig. 1a), which is another area where very large runups
695 were measured (see later for details of runups).

696 Surface elevation time series were simulated for the 8 scenarios, combining the four
697 volumes and two rheologies, at the locations of the 4 tide gauges (6-9 in Fig. 1a; Table 3), which
698 are compared to the measured detided surface elevations in Fig. 10. Unlike in the near-field, only
699 small differences (including on arrival time) can be seen here between surface elevations simulated
700 for the 8 different scenarios, indicating that the predictions of the tsunami far-field and impact are
701 less sensitive to details of the collapse scenario assumed for AK (i.e., changes in volume
702 size/geometry and rheology). This was already pointed out by other authors in their discussion of
703 model results (e.g., Heidarzadeh et al., 2020a; Borrero et al., 2020), and also explains why studies
704 that assumed an approximate empirical source for AK's collapse or only a 2D two-layer slide
705 model, with source parameters adjusted to match far-field data at the tide gauges and/or elsewhere,
706 performed reasonably well for predicting coastal impact. However, for future hypothetical
707 collapses, in the total absence of field data to calibrate these models, they might not have fared as
708 well in predicting tsunami impact, from a single forward model simulation.

709 Comparing numerical simulations to tide gauge data, Fig. 10 shows, overall, a good
710 agreement for any scenario, particularly earlier in the time series and more so for WG 6-8 (Figs.
711 10a-c). As summarized in Table 3, arrival times of the leading crest at each gauge are predicted to
712 within 15–78 s of observations. Considering the 1 minute data sampling interval of the gauges,

713 this is an acceptable discrepancy. Later in each tide gauge time series, the phase difference between
714 simulations and observations increases, but the trough-to-crest height of the largest waves are well
715 predicted in the simulations. As previously indicated, later in time, the signal at the tide gauges
716 was increasingly affected by local effects and seiching not resolved and simulated in Grid G1, both
717 due to the limited 50 m resolution and the moderately coarse 100 m resolution of the available
718 nearshore bathymetry and topography. Finally, as reported by eyewitnesses, simulations predict
719 that multiple large waves of fairly short period (2–10 minute) impacted the coast, with the second
720 or later waves being the largest.

721 For each of the 8 scenarios, arrival time at the tide gauges is, to the first-order, governed
722 by wave celerity, which strongly depends on bathymetry and to some extent on frequency for
723 dispersive waves. An additional effect of amplitude dispersion may speed-up wave propagation
724 for the largest waves in the near-field, but this effect will also be similar for all scenarios, as their
725 near-field waves are quite similar (see Fig. 6). This explains the small range in arrival time
726 difference, with the field data listed in Table 3 for the 8 scenarios.

727

728 4.4 *Near-field runups*

729 Grilli et al. (2019) pointed out the intense and continuous phreatomagmatic explosive activity that
730 immediately followed the collapse of AK, both obscuring the skies and discharging large volumes
731 of material that rapidly modified the post-collapse topography of AK and surrounding bathymetry.
732 Hunt et al. (2021) made a detailed analysis of these early stages of AK's post-collapse regrowth,
733 using both satellite images and submarine surveys, and quantified the large changes that took place
734 in AK's coastline and subaerial geometry (e.g., such as Fig. S1b and S1e for AK; see also
735 Novellino et al., 2020). This post-collapse eruptive activity paused on Jan. 11th 2019, and Reynolds

(2019) was able to conduct a drone survey of AK and the islands of Rakata, Sertung and Panjang (e.g., Fig. S1f and supplementary 4 in Grilli et al., 2019), that confirmed AK's coastline changes inferred from SAR images. Arguably more important was their documentation of the large runups the tsunami caused on the island of Rakata, Sertung and Panjang. Based on these images, Grilli et al. (2019) estimated that 50+ m runups occurred on Rakata's N shore and Sertung's S shore. Subsequent field surveys in 02/2019 by Borrero et al. (2020) and August 2019 by the authors confirmed and quantified these early observations of near-field tsunami impact, and provided geo-localized runup values reaching 80-85+ m on both islands (Fig. 11), with additional data on Panjang. However, because Panjang was positioned downwind of AK, extensive ashfall-driven vegetation damage, combined with the steep cliffs on the W coast (see white line in Fig. 11b) made the runup line on Panjang difficult to unambiguously identify. Finally, Borrero et al. (2020) also measured runup on Sebesi island, north of Panjang, which we also consider to be part of the near-field tsunami impact (Fig. 1a).

For the likeliest collapse volume scenario, with granular material, Figures 12a-c show zoom-ins of the maximum envelope of surface elevation computed with NHWAVE (Fig. 8) onto the NW shore of Rakata, SW shore of Sertung and S shore of Panjang, and Fig. 12d shows a zoom-in on Sebesi of the maximum envelope of surface elevation computed with FUNWAVE for the same scenario (Fig. 9d). The location of our August 2019 drone tree line survey is marked on Figs. 12a,b, and the location of four runups/flow depth measurements made on Sebesi by Borrero et al. (2019) are marked on Fig. 12d (7.5, 9, 2.8, 2.5 m from W to E, respectively); the latter values are consistent with those we estimated during our August 2019 survey of Sebesi, in part based on interviewing eyewitnesses. On both Rakata and Sertung (Figs. 12a,b), our predicted runup line touches or goes over the 50 m contour and parallels the drone survey quite well, except at its

highest points; those however occur on steep, nearly vertical, cliff faces (Figs. 11a,c) that are not well resolved with a 30 m horizontal grid. On Panjang, in Fig. 12c, our results show runups of 25-30 m on the island's SW tip, tapering to 8-10 m on the NW part of the western shore; the latter values match those reported by Borrero et al. (2020), who could not make a precise survey due to the difficulty in accessing the island, which is faced by steep cliffs on much of its western side (Fig. 11b). In Fig. 12d, our model results show a close agreement with the 4 measured runups on Sebesi's S and SE shore.

Figure 13 details the near-field runups computed on the 3 islands for the 8 modeled scenarios (4 volumes and 2 rheologies), compared to available runup measurements and our drone surveys. Overall, on Rakata and Sertung (Figs 13a,b), although all scenarios fare quite well, the likeliest volume scenario with a granular rheology appears to best match the quantitative field data, as well as images from the 01/11/2019 and Borrerro's et al.'s (2020) 02/2019 field survey (Figs. 11d,e) of these islands. On Panjang (Fig. 13c), all our model results are below our tree line drone survey (Fig. 11b) but, again, this was done along a nearly vertical cliff face, a location where it was difficult to estimate the runup line precisely and which is not well-discretized in our model grid; hence, there is large uncertainty on both these runup measurements and their model simulation. We note that all scenarios predict an 8 m runup on the NW side of the island as was reported by Borrero et al. (2020).

4.5 *Far-field runups*

Far-field flow depth and runups were measured along the coasts most exposed to the tsunami in Java and Sumatra in several field surveys. The first one (TDMRC, 2019 took place in 01/2019, soon after the event) was the only such data available to Grilli et al. (2019) to validate their

782 modeling. However, field surveys were also later performed by Muhari et al. (2019), Putra et al.
783 (2020), Borrero et al. (2020), and Heidarzadeh et al. (2020b). Figures 14 to 16 compare model
784 results obtained for the likeliest collapse scenario (granular rheology) with this data which, to our
785 knowledge, is all such data available to date.

786 Figure 14 shows a zoom-in along the coast of Java (Fig. 1a) on the envelope of maximum
787 surface elevation computed with FUNWAVE (Fig. 9d). As detailed in the methods section, both
788 the maximum flow depth at the shore and the runup were extracted from these results and, for
789 clarity, color coded in 4 classes of surface elevation. Due to the complex geometry of the coast,
790 the same values of flow depth and runup were then plotted as a function of longitude and latitude
791 in 4 subfigures (Figs. 14a,b,d,e); on the plan view (Fig. 14c), the color coded flow depth values
792 were plotted along the shore. Fig. 14c shows that, as expected from the tsunami directionality,
793 wave guiding effects offshore, and wave refraction nearshore, leading to focusing/defocusing
794 effects, the alongshore variation of maximum tsunami impact is a highly irregular on SW Java;
795 this causes similarly large alongshore variations in flow depth and runup seen in Figs. 14a,b,d,e.
796 The field data for both flow depth and runup is plotted on top of the elevation figures showing
797 model results, in Figs. 14b,d and. 14a,e, respectively. Overall, there is good agreement of model
798 results with the field measurements, and more so for flow depth at the coast, which is less sensitive
799 to irregularities of the terrain and the built-up elevation maps, that are not represented in our 50 m
800 resolution grid.

801 Figure 15 shows zoom-ins of results presented in Fig. 14 in three of the most impacted
802 areas along the coast of Java where field surveys were conducted, namely (Fig. 1a): (PI) Panaitan
803 Island; (UK) Ujung Kulon; and (K) Kolijaah. Model results for the likeliest volume scenario
804 (granular rheology) are compared to the locations/values of measured maximum runups, wherever

available (Fig. 15e), or otherwise to field data measured by Borrero et al. (2020) marked onto Google Earth images of each site (Figs. 15b,d). These measurements were provided as raw or detided, so here we are plotting their raw values compared to our results with respects to MWL. [Note, Borrero et al. only assumed a 2 cm tide throughout without justification, which will introduce some uncertainty in the comparison; also, their measurements from UK (Fig. 15d) are reported on Figs 14a,e as runup, since these values were measured inland.] At PI (Figs. 15a,b), the model accurately predicts the 6-8.4 m (referred to MWL) maximum tsunami elevations measured at the marked locations along an approximate N to S survey from the tip of the island (Fig. 15b; Borrero et al., 2020). At UK (Figs 15c,d) the model predicts slightly less (6.5 to 9 m) than the 6.9-11.5 m range (referred to MWL) of maximum tsunami heights measured at the marked locations from N to S from the tip of the Peninsula (Fig. 15d; Borrero et al, 2020); however, the largest flow depth was measured at an isolated tree (their Fig. 12) and our 50 m resolution model grid cannot represent this level of detail. Finally, at K (Figs. 15e,f) the model predicts most of the runups (both location and value) measured by Muhari et al. (2019), Putra et al. (2020), and Heidarzadeh et al. (2020b), reasonably well. Some of the reported measurement locations show a mismatch, but the majority of measured runups in the 3 surveys align well with our predicted inundation limit. At the K location, the Google Earth image (Fig. 15f) is only provided for reference.

Figure 16 shows results similar to those of Figure 14, for flow depth at the coast predicted along the SW shore of Sumatra for the likeliest collapse volume scenario (granular rheology), compared to the available data from field surveys; the agreement between both is quite good here as well. The largest tsunami impact occurred in the area of Waymuli (W in Fig. 1a, around

827 105.6348 E), of which Fig. 16c shows a picture of the damage taken by Fritz et al. (2019) during
828 their 02/2019 survey.
829
830 **5 Discussion and conclusions**.
831 New numerical simulations of AK's 2018 collapse and tsunami generation, propagation,
832 and coastal impact were performed with state-of-the-art numerical models, including a novel
833 landslide tsunami model for granular and viscous slides that includes non-hydrostatic effects of
834 vertical acceleration in the slide material. Results show that incorporating non-hydrostatic effects
835 is important for accurately simulating tsunami generation and near-field impacts from the AK flank
836 collapse. This is illustrated in the 8 scenarios we used, which combined 2 different rheologies
837 (granular and viscous fluid material) and 4 different volumes obtained from a new parametrization
838 of the collapse based on our August 2019 marine hydroacoustic survey (cf. Hunt et al., 2021), field
839 observations and new interpretations of high-resolution satellite imagery.
840 Based on our improved knowledge/understanding of subaerial and submarine data, from
841 which we better constrained the geometry and magnitude of the landslide mechanism, we also
842 improved on previous interpretations of the primary landslide scar, which bisected the Anak
843 Krakatau edifice, cutting behind the central vent and removing 50% of its subaerial volume. The
844 combined subaerial and marine datasets presented in Hunt et al. (2021) are used to provide a better
845 validated estimate of the landslide failure volume. From this, the failure volume is estimated to lie
846 within a range of 0.175 to 0.313 km^3, spanning the independently estimated deposit volume of
847 0.214 km^3. Given uncertainties in the precise form of the failure plane, the likeliest failure volume
848 of 0.224 km^3 is defined based on the submarine blocky deposit volume, mapped in the deep basin
849 to the SW of AK (0.214 ± 0.036 km^3) and allowing for an additional contribution from a much

850 smaller volume (0.022 ± 0.006 km^3) secondary debris flow deposit also mapped SW of the main
851 blocky deposit. Alongside this, we also model three additional failure scenarios encompassing the
852 minimum and maximum bounds of the landslide failure surface and geometry, with the 4 collapse
853 scenario geometries having volumes between 0.175 and 0.313 km^3.

854 Observations of a single tsunami wave train, with no subsequently generated waves, are
855 consistent with our interpretation from the marine surveys of landslide failure as a rapid, single
856 phase, *en masse* movement, rather than a more piecemeal process; in the seafloor deposits, there
857 is indeed no evidence that the slide volume was divided among multiple-stages of failure (Hunt et
858 al., 2021). A single event interpretation is also supported by the marine seismic data. Thus, unlike
859 the collapses at larger volcanic islands (e.g., Canaries; Hunt et al., 2011), single-stage failures that
860 maximize the volume of material available at any one time for tsunamigenesis appear to be more
861 the norm in settings such as AK's.

862 In the context of the many uncertainties in field observations, all our volume scenarios
863 successfully reproduced the near- and far-field tsunami flow depths and runups observed in all
864 post-event field survey results published to date, as well as arrival times and time series of surface
865 elevations at tide gauges, and from eyewitness reports. This match between our model results and
866 field observations confirms that our estimated landslide volume range and material rheologies are
867 appropriate to the collapse event. Note, however, that slide dilation, an important physical aspect,
868 which results from water being sucked into the granular material during slide motion, is not
869 included in NHWAVE. While this effect could affect tsunami generation, the good agreement
870 observed in the near-field between the measured and predicted runups would indicate that this was
871 not significant during AK's event. Additionally, the many large blocks seen in the debris deposits
872 would indicate that the amount of interstitial water may have been smaller than assumed in

873 simulations and that actual dilation effects were minor. Nevertheless dilation would be important
874 to include in the model and study in future work.

875 Despite an observed moderate sensitivity of tsunami impact to the range of modeled
876 landslide sources, particularly in the far-field, the granular rheology appears to yield slide deposits
877 in better agreement with the marine deposits mapped in the 2019 survey (both location and
878 thickness) than those from the dense fluid rheology. Additionally, near-field runups are also better
879 predicted using a granular rheology. Regarding the collapse volume, the likeliest value inferred
880 from the 2019 field survey, together with a refined analysis of satellite images, is 0.224 km^3
881 (referred to in this paper as the likeliest scenario), which appears to provide the overall best
882 agreement with the near-field runup measurements, as well as the far-field data. Hence, while the
883 volume is harder to constrain using far-field data, we conclude that tsunami modeling supports the
884 likeliest scenario inferred from the 2019 marine geology survey, although the constraint is weaker
885 than for the rheology.

886 The AK event highlights the significant hazard posed by relatively small-scale lateral
887 volcanic collapses, which occur *en-masse*, without any readily identified 'predictive', precursory
888 signals, and are an efficient and unpredictable tsunami source. Our successful simulations
889 demonstrate that current numerical models can accurately forecast tsunami hazards from these
890 events, even assuming a large uncertainty on the source parameters (e.g., collapse failure plane
891 and volume); this is why Giachetti et al. (2012)'s work provided a reasonable forecast of the event
892 that took place at AK in 2018.

893 In cases such as AK's, the absence of precursory warning signals of imminent collapse
894 together with the short travel time following tsunami initiation present a major challenge for
895 mitigating tsunami coastal impact from volcanic sources, stressing the need to install early warning

systems. After the AK 2018 event, using ground- and space-borne data, Walter et al. (2019) identified thermal anomalies and a gradual seaward motion of the volcano that they suggested could be used as precursors of the collapse. A warning system could thus closely monitor volcanoes exhibiting and elevated sate of activity for such precursor signs. Warning systems could also use instruments allowing for an early detection of the tsunami generated by the collapse. Mulia et al. (2020) suggested that a high frequency (HF) radar could have been useful in providing an early detection of the tsunami generated by AK's collapse. In fact, Grilli et al. (2016, 2017a) proposed new algorithms for processing HF radar data to efficiently detect tsunami signals; by performing model simulations similar to those reported here, they demonstrated that their algorithm could provide an early detection of landslide tsunamis. Guérin et al. (2018) later applied this method to detect a meteo-tsunami/surge using actual HF radar data, off of Toffino, BC. Another novel approach recently proposed for detecting sea surface variations, such as those caused by non-seismic tsunamis, is that based on Coastal Global Navigation Satellite Systems (GNSS) signal reflection on the sea surface (e.g., Larson et al., 2020).

Data sharing

A shared Google Drive folder containing all the NHWAVE and FUNWAVE model input data as well as all raw results generated for the simulations of the 2018 AK collapse and tsunami reported in this paper is accessible at: https://drive.google.com/drive/folders/1-60PsB3Zj-P58rbbAdbWUZ611I_QMs2S?usp=sharing.

Acknowledgements

STG, CZ and JTK acknowledge support from grants CMMI-1535568 to the University of Rhode Island and CMMI-1537232 to the University of Delaware from the United States (US) National Science Foundation (NSF). Computational resources were provided by University of Delaware Instructional Technology. STG and ARG acknowledge support from NSF grant GEO-17-56665. National Environmental Research Council (NERC) grant NE/S003509/1 is acknowledged by DRT, SW and SE, and Grant NE/T002026/1 by SW, SE, MC and MA. JEH recognizes NERC Urgency Grant NE/T002034/1. DRT, AN and SE publish with permission of the CEO, British Geological Survey. COSMO-SkyMed (CSK) data was provided by the Italian Space Agency through the Committee on Earth Observation Satellite's Earth Observation (CEOS)'s Volcano Demonstrator (Order ID: 740794). FUNWAVE-TVD is open source software available at http://github.com/fengyanshi/FUNWAVE-TVD/. NHWAVE is open source software available at http://github.com/jimkirby/nhwave/. The Indonesian Ministry of Marine Affairs and Fisheries (http:/tides.big.go.id) is gratefully acknowledged for providing the authors with tide-gauge data, and Dr. Raphael Paris for providing bathymetry/topography data. Jose Borrero from eCoast Marine Consulting and Research is gratefully acknowledged for providing the pictures shown in Figs. 11d and e.

References

1. Abadie, S.M., Harris, J.C., Grilli, S.T. & Fabre, R. (2012). Numerical modeling of tsunami waves generated by the flank collapse of the Cumbre Vieja Volcano (La Palma, Canary Islands): Tsunami source and near field effects. Journal of Geophysical Research, vol. 117, pp. C05030, doi:10.1029/2011jc007646.
2. Abadie, S., Paris, A., Ata, R., Le Roy, S., Arnaud, G., Poupardin, A., Clous, L., Heinrich, P., Harris, J., Pedreros, R. and Krien, Y. (2020). La Palma landslide tsunami: calibrated wave source and assessment of impact on French territories. Natural Hazards and Earth System Sciences, vol. 20, no. 11, pp. 3019-3038, doi:10.5194/nhess-20-3019-2020.
3. Abdurrachman, M., Widiyantoro, S., Priadi, B., Ismail, T. (2018). Geochemistry and Structure of Krakatoa Volcano in the Sunda Strait, Indonesia. Geosciences, vol. 8, pp. 111.
4. AGU blog 2019. Anak Krakatau: Planet Labs imagery of the aftermath of the landslide. Accessed Jan. 3, 2019. https://blogs.agu.org/landslideblog/2019/01/03/anak-krakatau-3/?utm_source=AGU+Blogosphere+-+The+Landslide+Blog&utm_campaign=0979aaaa17-RSS_EMAIL_CAMPAIGN_LANDSLIDE&utm_medium=email&utm_term=0_b2461e255e-0979aaaa17-555513653
5. AHA, C. (2018). Indonesia, Tsunami in Sunda Strait, http://adinet.ahacentre.org/reports/view/1383. First accessed Dec. 23, 2018.
6. Andersen, O. (2018). Krakatau Volcano: Witnessing the eruption, tsunami and the aftermath 22-23th December 2018, Accessed on December 26, 2018. http://www.oysteinlundandersen.com/krakatau-volcano-witnessing-the-eruption-tsunami-22december2018/.
7. Anon (2018). Global Volcanic Program, in: Venzke, E. (Ed.), Bulletin of the Global Volcanism Network. Smithsonian Institution, Washington.

8. Auker, M.R., Sparks, R.S.J., Siebert, L., Crosweller, H.S., Ewert, J. (2013). A statistical analysis of the global historical volcanic fatalities record. Journal of Applied Volcanology, vol. 2, pp. 1-24, doi:10.1186/2191-5040-2-2.
9. Borrero, J.C., T. Solihuddin, H.M. Fritz, P.J. Lynett, G.S. Prasetya, D. Purbani, H.L Salim et al. (2020). Field Survey and Numerical Modelling of the December 22, 2018 Anak Krakatau Tsunami. Pure and Applied Geophys., vol. 177, pp. 2457-2475, doi:10.1007/s00024-020-02515-y
10. Camus, G., Gourgaud, A., Vincent, P.M. (1987). Petrologic evolution of Krakatau (Indonesia): Implications for a future activity. Journal of Volcanology and Geothermal Research, vol. 33, pp. 299-316, doi:10.1016/0377-0273(87)90020-5.
11. Day, S.J., P. Watts, S.T. Grilli and Kirby J.T. (2005). Mechanical Models of the 1975 Kalapana, Hawaii Earthquake and Tsunami. Marine Geology, vol. 215, no. 1-2, pp. 59-92, doi:10.1016/j.margeo.2004.11.008.
12. Day, S. (2015). Volcanic tsunamis, The Encyclopedia of Volcanoes. Elsevier, pp. 993–1009.
13. Day, S., Lanes, P., Silver, E., Hoffmann, G., Ward, S., Driscoll, N. (2015). Submarine landslide deposits of the historical lateral collapse of Ritter Island, Papua New Guinea. Marine and Petroleum Geology, vol. 67, pp. 419-438, doi:10.1016/j.marpetgeo.2015.05.017.
14. Deplus, C., S. Bonvalot, D. Dahrin, M. Diament, H. Harjono, and J. Dubois (1995). Inner structure of the Krakatau volcanic complex (Indonesia) from gravity and bathymetry data. J. Volcan. Geotherm. Res., vol. 64, no. 1-2, pp. 23-52, doi:10.1016/0377-0273(94)00038-I.
15. Dogan, G.G., Annunziato, A., Hidayat, R., Husrin, S., Prasetya, G., Kongko, W., Zaytsev, A., Pelinovsky, E., Imamura, F. and Yalciner, A.C. (2021). Numerical Simulations of December 22, 2018 Anak Krakatau Tsunami and Examination of Possible Submarine Landslide Scenarios. Pure and Applied Geophysics, pp.1-20, doi:10.1007/s00024-020-02641-7.
16. Fritz et 16 alii (2019). The 2018 Anak Krakatau tsunami: Near-source field survey on Islands in the Sunda Strait. Presentation at Intl. Symp. on the Lessons Learnt from the 2018 Tsunamis in Palu and Sunda Strait, 26-28 September 2019, Auditorium BMKG, Jakarta – Indonesia.

17. Fornaciai, A., Favalli, M. and Nannipieri, L. (2019). Numerical simulation of the tsunamis generated by the Sciara del Fuoco landslides (Stromboli Island, Italy). Scientific reports, vol. 9, no. 1, pp. 1-12, doi: 10.1038/s41598-019-54949-7.
18. Giachetti, T., Paris, R., Kelfoun, K., Pérez-Torrado, F.J. (2011). Numerical modelling of the tsunami triggered by the Güìmar debris avalanche, Tenerife (Canary Islands): Comparison with field-based data. Marine Geology, vol. 284, pp. 189-202, doi:10.1016/j.margeo.2011.03.018.
19. Giachetti, T., Paris, R., Kelfoun, K., Ontowirjo, B. (2012). Tsunami hazard related to a flank collapse of Anak Krakatau Volcano, Sunda Strait, Indonesia. Geological Society, London, Special Publications, vol. 361, pp. 79-90.
20. Glimsdal, S., Pedersen, G. K., Harbitz, C. B., and Løvholt, F. (2013). Dispersion of tsunamis: does it really matter? Natural hazards and earth system sciences, vol. 13, no. 6, pp. 1507-1526, doi: 10.5194/nhess-13-1507-2013.
21. Gouhier, M. and Paris, R (2019). SO2 and tephra emissions during the December 22, 2018 Anak Krakatau eruption. Volcanica, vol. 2, no. 2, pp. 91-103, doi: 10.30909/vol.02.02.91103.
22. Grilli, S.T., Ioualalen, M, Asavanant, J., Shi, F., Kirby, J. and Watts, P. (2007). Source Constraints and Model Simulation of the December 26, 2004 Indian Ocean Tsunami. Journal of Waterway Port Coastal and Ocean Engineering, vol. 133, no. 6, pp. 414-428, doi:10.1061/(ASCE)0733-950X(2007)133:6(414).
23. Grilli, S.T. J.C. Harris, T. Tajalibakhsh, T.L. Masterlark, C. Kyriakopoulos, J.T. Kirby and F. Shi (2013). Numerical simulation of the 2011 Tohoku tsunami based on a new transient fem co-seismic source: Comparison to far- and near-field observations. Pure and Applied Geophysics, vol. 170, pp. 1333–1359, doi:10.1007/s00024-012-0528-y.
24. Grilli, S.T., O'Reilly, C., Harris, J.C., Tajelli-Bakhsh, T., Tehranirad, B., Banihashemi, S., Kirby, J.T., Baxter, C.D.P., Eggeling, T., Ma, G., and F. Shi (2015). Modeling of SMF tsunami hazard along the upper US East Coast: detailed impact around Ocean City, MD. Natural Hazards, vol. 76, pp. 705-746; doi:10.1007/s11069-014-1522-8.

25. Grilli, S.T., Grosdidier S. and C.-A. Guérin (2016). Tsunami detection by High Frequency Radar beyond the continental shelf. I. Algorithms and validation on idealized case studies. Pure and Applied Geophysics, vol. 173, no. 12, pp. 3,895-3,934, doi:10.1007/s00024-015-1193-8
26. Grilli, S.T., Guérin, C.-A., Shelby, M., Grilli, A., P. Moran, Grosdidier, S. and T.L. Insua (2017a). Tsunami detection by High Frequency Radar beyond the continental shelf: II. Extension of algorithms and validation on realistic case studies. Pure and Appl. Geophys., vol. 174, no. 1, pp. 3,003-3,028, doi:10.1007/s00024-017-1619-6.
27. Grilli, S.T., Shelby, M., Kimmoun, O., Dupont, G., Nicolsky, D., Ma, G., Kirby, J.T. and F. Shi (2017b). Modeling coastal tsunami hazard from submarine mass failures: effect of slide rheology, experimental validation, and case studies off the US East coast. Natural Hazards, vol. 86(1), pp. 353-391, doi:10.1007/s11069-016-2692-3.
28. Grilli, S.T., Tappin, D.R., Carey, S., Watt, S.F.L., Ward, S.N., Grilli, A.R., Engwell, S.L., Zhang, C., Kirby, J.T., Schambach, L., Muin, M. (2019). Modelling of the tsunami from the December 22, 2018 lateral collapse of Anak Krakatau volcano in the Sunda Straits, Indonesia. Scientific Reports, vol. 9, no. 11946, doi:10.1038/s41598-019-48327-6.
29. Guérin C.-A., S.T. Grilli, P. Moran, A.R. Grilli, T.L. Insua (2018). Tsunami detection by High Frequency Radar in British Columbia: performance assessment of the Time-Correlation Algorithm for synthetic and real events. Ocean Dynamics, 68(4-5), pp. 423-438, doi:10.1007/s10236-018-1139-7.
30. Gurney, J. (2018) Low frequency analysis of the 13:55 event (arrival at Bungbulang at 13:57 UTC), UK Earthquake Bulletin.
31. Heidarzadeh, M., Ishibe, T., Sandanbata, O., Muhari, A., Wijanarto, A.B. (2020a). Numerical modeling of the subaerial landslide source of the 22 December 2018 Anak Krakatoa volcanic tsunami, Indonesia. Ocean Engineering, vol. 195, no. 106733.

1033 32. Heidarzadeh, M., Putra, P. S., Nugroho, S. H., and Rashid, D. B. Z. (2020b). Field survey of tsunami
1034 heights and runups following the 22 December 2018 Anak Krakatau volcano tsunami, Indonesia. Pure
1035 and Applied Geophysics, vol. 177, no. 10, pp. 4577-4595, doi: 10.1016/j.oceaneng.2019.106733
1036 33. Hunt, J.E., Wynn, R.B., Masson, D.G., Talling, P.J., Teagle, D.A.H. (2011). Sedimentological and
1037 geochemical evidence for multistage failure of volcanic island landslides: A case study from Icod
1038 landslide on north Tenerife, Canary Islands. Geochem. Geophys. Geosyst., vol. 12, no. Q12007, doi:
1039 10.1029/2011GC003740
1040 34. Hunt, J.E., Tappin, D.R., Watt, S.F., Susilohadi, S., Novellino, A., Ebmeier, S.K., Cassidy, M.,
1041 Engwell, S.L., Grilli, S.T., Hanif, M., Priyanto, W.S., Clare, M.A., Abdurrachman, M., Udrekh, U.
1042 (2021). Submarine landslide megablocks show half the island of Anak Krakatau failed on December
1043 22nd, 2018. Nature Communication, vol. 12, no. 2827, doi:10.1038/S41467-021-22610-5.
1044 35. Imamura, F. and Imteaz, M.M.A. (1995). Long waves in two-layers: Governing equations and
1045 numerical model. Science of Tsunami Hazards, vol. 13, no. 1, pp. 3-24.
1046 36. Ina-COAP (2019). *Tide Gauge data in Indonesia*, http://tides.big.go.id/las/UI.vm Accessed Jan. 3,
1047 2019.
1048 37. Ioualalen, M., Asavanant, J., Kaewbanjak, N., Grilli, S.T., Kirby, J.T. and P. Watts (2007). Modeling
1049 the 26th December 2004 Indian Ocean tsunami: Case study of impact in Thailand. Journal of
1050 Geophysical Research, vol. 112, pp. C07024, doi:10.1029/2006JC003850.
1051 38. Johnson, R.W., (1987). Large-scale volcanic cone collapse: the 1888 slope failure of Ritter Volcano,
1052 and other examples from Papua New Guinea. Bulletin of Volcanology, vol. 49, pp. 669–679, doi:
1053 10.1007/BF01080358.
1054 39. Karstens, J., Berndt, C., Urlaub, M., Watt, S.F.L., Micallef, A. et al. (2019). From gradual spreading to
1055 catastrophic collapse – Reconstruction of the 1888 Ritter Island volcanic sector collapse from high-
1056 resolution 3D seismic data. Earth and Planetary Science Letters, vol. 517, pp. 1-13, doi:
1057 10.1016/j.epsl.2019.04.009

40. Kirby, J.T., Shi, F., Tehranirad, B., Harris, J.C. and Grilli, S.T. (2013). Dispersive tsunami waves in the ocean: Model equations and sensitivity to dispersion and Coriolis effects. Ocean Modeling, vol. 62, pp. 39-55, doi:10.1016/j.ocemod.2012.11.009.

41. Kirby, J.T., Shi, F., Nicolsky, D., and S. Misra (2016). The 27 April 1975 Kitimat, British Colombia, submarine landslide tsunami: a comparison of modeling approaches. Landslides, vol. 13, no. 6, pp. 1421-1434 doi: 10.1007/s10346-016-0682-x.

42. Larson, K. M., Lay, T., Yamazaki, Y., Cheung, K. F., Ye, L., Williams, S. D. and Davis, J. L. (2021). Dynamic sea level variation from GNSS: 2020 Shumagin earthquake tsunami resonance and Hurricane Laura. Geophysical Research Letters, vol. 48, no. 4, e2020GL091378, doi: 10.1029/2020GL091378 .

43. Løvholt, F., Pedersen, G., Gisler, G. (2008). Oceanic propagation of a potential tsunami from the La Palma Island. Journal of Geophysical Research, vol. 113, no. C09026, doi:10.1029/2007JC004603.

44. Ma, G., Shi, F., and Kirby, J.T. (2012). Shock-capturing non-hydrostatic model for fully dispersive surface wave processes. Ocean Modelling, vol. 43-44, pp. 22-35, doi:10.1016/j.ocemod.2011.12.002.

45. Ma, G., Kirby, J.T., Hsu, T.J., and Shi, F. (2015). A two-layer granular landslide model for tsunami wave generation: theory and computation. Ocean Modelling, vol. 93, pp. 40-55, doi:10.1016/j.ocemod.2015.07.012.

46. Muhari, A. (2018). in *Kompas*, (in Indonesian) https://sains.kompas.com/read/2018/12/23/180319123/menyoal-dakwaan-pada-anak-krakatau-tentang-kasus-tsunami-selat-sunda?page=all. Accessed Dec. 23, 2018.

47. Muhari, A., Heidarzadeh, M., Susmoro, H., Nugroho, H.D., Kriswati, E., Wijanarto, A.B., Imamura, F. and Arikawa, T. (2019). The December 2018 Anak Krakatau volcano tsunami as inferred from post-tsunami field surveys and spectral analysis. Pure and Applied Geophysics, vol. 176, no. 12, pp. 5219-5233, doi: https:10.1007/s00024-019-02358-2.

48. Mulia, I.E., Watada, S., Ho, T.-C., Satake, K., Wang, Y., Aditiya, A. (2020). Simulation of the 2018 Tsunami Due to the Flank Failure of Anak Krakatau Volcano and Implication for Future Observing Systems. Geophysical Research Letters, vol. 47, no. e2020GL087334, doi:10.1029/2020GL087334.

1084 49. Neumann van Padang, M. (1983). History of the volcanology in the former Netherlands East Indies.
1085 *Rijksmuseum van Geologie en Mineralogie*.
1086 50. Novellino, A., Engwell, S.L., Grebby, S., Day, S., Cassidy, M., Madden-Nadeau, A., Watt, S., Pyle,
1087 D., Abdurrachman, M., Edo Marshal Nurshal, M. and Tappin, D.R. (2020). Mapping recent shoreline
1088 changes spanning the lateral collapse of Anak Krakatau Volcano, Indonesia. Appl. Sci., vol. 10, no. 2,
1089 pp. 536, doi: 10.3390/app10020536.
1090 51. Omira, R. and Ramalho, I. (2020). Evidence-Calibrated Numerical Model of December 22, 2018, Anak
1091 Krakatau Flank Collapse and Tsunami. Pure and Applied Geophysics, vol. 177, no. 7, pp. 3059-3071,
1092 doi: 10.1007/s00024-020-02532-x.
1093 52. Paris, R. (2015). Source mechanisms of volcanic tsunamis. Philosophical Transactions of the Royal
1094 Society of London A: Mathematical, Physical and Engineering Sciences, vol. 373, no. 2053, pp.
1095 20140380, doi: 10.1098/rsta.2014.0380.
1096 53. Paris, A., Heinrich, P., Paris, R., and Abadie, S. (2020a). The December 22, 2018 Anak Krakatau,
1097 Indonesia, landslide and tsunami: preliminary modeling results. Pure and Applied Geophysics, vol.
1098 177, no. 2, pp. 571-590, doi: 10.1007/s00024-019-02394-y
1099 54. Paris, R., Goto, K., Goff, J. and Yanagisawa, H. (2020b). Advances in the study of mega-tsunamis in
1100 the geological record. Earth-Science Reviews, no. 103381, doi:10.1016/j.earscirev.2020.103381.
1101 55. Perttu, A., Caudron, C., Assink, J.D., Metz, D., Tailpied, D., Perttu, B., Hibert, C., Nurfiani, D., Pilger,
1102 C., Muzli, M. and Fee, D. (2020). Reconstruction of the 2018 tsunamigenic flank collapse and eruptive
1103 activity at Anak Krakatau based on eyewitness reports, seismo-acoustic and satellite
1104 observations. Earth and Planetary Science Letters, vol. 541, pp.116268, doi:
1105 10.1016/j.epsl.2020.116268.
1106 56. Putra, P. S., Aswan, A., Maryunani, K. A., Yulianto, E., Nugroho, S. H., & Setiawan, V. (2020). Post-
1107 Event Field Survey of the 22 December 2018 Anak Krakatau Tsunami. Pure and Applied Geophysics,
1108 vol. 177, pp. 2477–2492, doi:10.1007/s00024-020-02446-8

57. PVMBG (2018). Activity reports for Anak Krakatau from 01/12/2018 – 03/01/2019. Pusat Vulkanologi dan Mitigasi Bencana Geologi.

58. Priyanto, W.S., Hunt, J.E., Hanif, M., Tappin, D.R., Permana, H., Susilohadi, S., Cassidy, M. and Yulianto, E. (2021). Bathymetry and Shallow Seismic Imaging of the 2018 Flank Collapse of Anak Krakatau. Frontiers in Earth Science, 8, pp. 649, doi:10.3389/feart.2020.577448.

59. Ren, Z., Wang, Y., Wang, P., Hou, J., Gao, Y., and Zhao, L. (2020). Numerical study of the triggering mechanism of the 2018 Anak Krakatau tsunami: eruption or collapsed landslide?. Natural Hazards, vol. 102, no. 1, pp. 1-13, doi:10.1007/s11069-020-03907-y.

60. Reynolds, J. (2019). *Post-collapse image of Anak Krakatau. Earth Uncut TV*, https://twitter.com/hashtag/Krakatau?src=hash, Accessed Jan. 11, 2019.

61. Schambach L., Grilli S.T., Kirby J.T. and F. Shi (2019). Landslide tsunami hazard along the upper US East Coast: effects of slide rheology, bottom friction, and frequency dispersion. Pure and Applied Geophys*ics*, vol. 176, no. 7, pp. 3,059-3,098, doi.org/10.1007/s00024-018-1978-7.

62. Schambach L., Grilli S.T., Tappin D.R., Gangemi M.D., and G. Barbaro (2020a). New simulations and understanding of the 1908 Messina tsunami for a dual seismic and deep submarine mass failure source, *Marine Geology*, vol. 421, pp. 106093, doi: 10.1016/j.margeo.2019.106093.

63. Schambach L., Grilli S.T. and D.R. Tappin (2020b). New high-resolution modeling of the 2018 Palu tsunami, based on supershear earthquake mechanisms and mapped coastal landslides, supports a dual source. Frontiers in Earth Sciences, vol. 8, pp. 627, doi:10.3389/feart.2020.598839.

64. Simkin, T., Fiske, R.S. (1983). Krakatau 1883: the volcanic eruption and its effects. Smithsonian Institution Press, Washington, D.C.

65. Siswowidjoyo, S. (1983). Krakatau, Symposium on 100 years development Krakatau its surroundings. Indonesian Inst. Sci. Jakarta, Jakarta, pp. 191–198.

66. Shi, F., Kirby, J.T., Harris, J.C., Geiman, J.D. and S.T. Grilli (2012). A high-order adaptive time-stepping TVD solver for Boussinesq modelling of breaking waves and coastal inundation. Ocean Modelling, vol. 43-44, pp. 36-51, doi:10.1016/j.ocemod.2011.12.004.

67. Stehn, C. (1929). The geology and volcanism of the Krakatau group, Krakatau, Proc. 4th Pacific Sci. Congr, Batavia I, pp. 1-55.

68. Tappin, D.R., Watts, P., Grilli, S.T. 2008. The Papua New Guinea tsunami of 1998: anatomy of a catastrophic event. Natural Hazards and Earth System Sciences, vol. 8, pp. 243-266, doi:www.nat-hazards-earth-syst-sci.net/8/243/2008/

69. Tappin, D.R., Grilli, S.T., Harris, J.C., Geller, R.J., Masterlark, T., Kirby, J.T., Shi, F., Ma, G., Thingbaijam, K.K.S., and P.M. Mai (2014). Did a submarine landslide contribute to the 2011 Tohoku tsunami? Marine Geology, vol. 357, pp. 344-361, doi:10.1016/j.margeo.2014.09.043.

70. TDMRC (Tsunami, D., and Mitigation, Research, Center) (2019). Post Sunda Strait Tsunami Survey. Tsunami, Disaster, and Mitigation, Research, Center, Jakarta. http://tdmrc.unsyiah.ac.id/thelatest-update-from-post-sunda-strait-tsunami-survey/. Accessed Jan. 8, 2019

71. Tehranirad B., Harris J.C., Grilli A.R., Grilli S.T., Abadie S., Kirby J.T. and F. Shi 2015. Far-field tsunami impact in the north Atlantic basin from large scale flank collapses of the Cumbre Vieja volcano, La Palma. Pure and Applied Geophysics, vol. 172, no. 12, pp. 3,589-3,616, doi:10.1007/s00024-015-1135-5.

72. Tinti, S., Pagnoni, G., and Zaniboni, F. (2006). The landslides and tsunamis of the 30th of December 2002 in Stromboli analysed through numerical simulations. Bull. Volcanol. 68, 462–479. doi:10.1007/839 s00445-005-0022-9.

73. Umbgrove, J. H. F. (1928). The first days of the new submarine volcano near Krakatoa. Leidse Geologische Mededelingen, vol. 2, no. 1, pp. 325-328.

74. Verbeek, R.D.M. (1885). Krakatau. Government Press Batavia.

75. Verbeek, R.D.M. (1983). Krakatau, in: Simkin, T., Fiske, R.S. (Eds.), Krakatau 1883: The Volcanic Eruption and its Effects. Smithsonian Press, Washington, D.C., pp. 169-277.

76. Walter, T.R., Haghighi, M.H., Schneider, F.M., Coppola, D., Motagh, M., Saul, J., Babeyko, A., Dahm, T., Troll, V.R., Tilmann, F. and Heimann, S., 2019. Complex hazard cascade culminating in the Anak Krakatau sector collapse. Nature communications, vol. 10, no. 4339.

77. Ward, S.N., Day, S. (2001). Cumbre Vieja volcano – Potential collapse and tsunami at La Palma, Canary Islands. Geophysical Research Letters, vol. 28, no. 17, pp. 3397– 3400, doi: 10.1029/2001GL013110.

78. Ward, S.N. and Day, S. (2003). Ritter Island Volcano-lateral collapse and the tsunami of 1888. Geophysical Journal International, vol. 154, pp. 891–902, doi: 10.1046/j.1365-246X.2003.02016.x.

79. Ward, S. N. and Day, S. (2006). Particulate kinematic simulations of debris avalanches: interpretation of deposits and landslide seismic signals of Mount Saint Helens, 1980 May 18. Geophysical Journal International, vol. 167, no. 2, pp. 991-1004.

80. Watt, S.F.L., Karstens, J., Micallef, A., Berndt, C., Urlaub, M., Ray, M., Desai, A., Sammartini, M., Klaucke, I., Böttner, C., Day, S., Downes, H., Kühn, M., Elger, J. (2019). From catastrophic collapse to multi-phase deposition: Flow transformation, seafloor interaction and triggered eruption following a volcanic-island landslide. Earth and Planetary Science Letters, vol. 517, pp. 135-147, doi: 10.1016/j.epsl.2019.04.024.

81. Williams, R., Rowley, P. and Garthwaite, M.C. (2019). Reconstructing the Anak Krakatau flank collapse that caused the December 2018 Indonesian tsunami. Geology, vol. 47, no. 10, pp. 973-976, doi: 10.1130/G46517.1.

82. Yavari-Ramshe, S., and Ataie-Ashtiani, B. (2016). Numerical simulation of subaerial and submarine landslide generated tsunami waves—recent advances and future challenges. Landslides, 13(6), pp. 1325–1368, doi: 10.1007/s10346-016-0734-2.

83. Ye, L., Kanamori, H., Rivera, L., Lay, T., Zhou, Y., Sianipar, D., and Satake, K. (2020). The 22 December 2018 tsunami from flank collapse of Anak Krakatau volcano during eruption. Sci. Advances, vol. 6, no. 3, pp. eaaz1377, doi:10.1126/sciadv.aaz1377.

84. Zengaffinen, T., Løvholt, F., Pedersen, G.K., Muhari, A. (2020). Modelling 2018 Anak Krakatoa Flank Collapse and Tsunami: Effect of Landslide Failure Mechanism and Dynamics on Tsunami Generation. Pure and Applied Geophysics, vol. 177, pp. 2493-2516, doi: 10.1007/s00024-020-02489-x.

85. Zhang C., Kirby J., Shi F., Ma G. and S.T. Grilli (2021a). A two-layer non-hydrostatic landslide model for tsunami generation on irregular bathymetry. 1. Theoretical basis. *Ocean Modelling*, vol. 159, no. 101749, doi:10.1016/j.ocemod.2020.101749.

86. Zhang C., Kirby J., Shi F., Ma G. and S.T. Grilli (2021b). A two-layer non-hydrostatic landslide model for tsunami generation on irregular bathymetry. 2. Numerical discretization and model validation. *Ocean Modelling,* vol. 160, no. 101769, doi:10.1016/j.ocemod.2021.101769.

Tables

Study/Paper	AK Collapse model	Tsunami model	Bathymetry Grid	AK Collapse source
Grilli et al. (2019)	NHWAVE: Multi-layer 3D Euler solver coupled with 2D layer slide model with dense viscous fluid/granular medium slide rheology	FUNWAVE: 2D fully nonlinear and dispersive Boussinesq model	NHWAVE: 90 m resolution Cartesian grid with 5 vertical layers; FUNWAVE: 100 m resolution Cartesian grid. Bathy/topo: 100 m resolution Giachetti et al. (2012)'s data	Geometry and failure surface reconstructed from pre-/post-collapse satellite observations, with volume of 0.22-0.30 km^3 (likeliest 0.27 km^3)
Zengaffinen et al. (2020)	BinClaw: 2D two-layer water/slide coupled with viscoplastic slide rheology	GeoClaw: 2D nonlinear and non-dispersive long wave model (NLSW) GloBous: 2D linear dispersive long wave model (LSW) for limited comparison	BinClaw: 36 m resolution Cartesian grid GeoClaw: 175 m resolution Cartesian grid Globous: 100 m resolution Cartesian grid Bathy/topo: Giachetti et al. (2012)'s data	Same 0.28 km^3 volume, geometry, and failure surface as in Giachetti et al. (2012)
Paris et al. (2020a)	AVALANCHE: 2D two-layer water/slide with granular medium slide rheology	2D weakly nonlinear and dispersive Boussinesq model	Coarse grids (180 m ?) over deep water and 25 m resolution around AK and in 5 nested coastal grids Bathy/topo: from Gouhier and Paris (2019)	Geometry and failure surface reconstructed from pre-/post-collapse satellite and aerial observations, with volume of 0.15 km^3
Ren et al. (2020)	2D two-layer water/slide coupled model with dense fluid slide rheology	GeoClaw: 2D nonlinear and non-dispersive long wave model (NLSW)	Generation: 30 m resolution nested grid GeoClaw: Coarse 0.125 arc-min (230 m) resolution grid Bathy/topo: interpolated from coarse 30 arc-sec (900 m) SRTM30_Plus data	Geometry and failure surface reconstructed from pre-/post-collapse satellite observations, with volume of 0.10-0.30 km^3 based on Grilli et al. (2019)
Mulia et al. (2020)	VolcFlow: 2D two-layer water/slide coupled model simulating silde with avalanche dynamics with retarding stress	FUNWAVE: 2D fully nonlinear and dispersive Boussinesq model	VolcFlow: 3 arc-sec (90 m) resolution grid FUNWAVE: 6 arc-sec (180 m) resolution grid Bathy/topo: 6 arc-sec bathymetry and 0.27 arc-sec topography around AK	Similar failure surface as in Giachetti et al. (2012) with steeper plane yielding a 0.24 km^3 volume
Heidarzadeh et al. (2020a)	No collapse/slide modeling. Empirical initialization based on laboratory experiments	COMCOT: 2D nonlinear and non-dispersive long wave model (NLSW)	Single 8 arc-sec (250 m) resolution grid Bathy/topo: from GEBCO-2014 30 arc-sec (900 m) resolution data	0.005 to 0.677 km^3 volume (empirical). Best fit with observations: 0.175 km^3 volume
Borrero et al. (2020)	No collapse/slide modeling. initialization with analytical solution	pCOULWAVE: 2D fully nonlinear and dispersive Boussinesq model	Single 2 arc-sec (60 m) resolution grid Bathy/topo: not defined	Analytical source parameters adjusted to best match the near-field runups
Omira and Ramalho, (2020)	2D Viscoplastic/ Bingham slide model with upper water layer solving Nonlinear Shallow Water Eqs.	Same NSW model as slide model used for tsunami propagation.	Grid resolution not specified, Bathy/topo: DEMNAS 10 m topography and BIG 5 m bathymetry. A 10 m DEM is interpolated from both.	Two-failure sequence at 5 s, with 0.135 km^3 total volume, geometry reconstructed from pre-/post-collapse satellite observations
Dogan et al. (2021)	2D two-layer water/slide coupled model with dense fluid slide rheology	NAMI DANCE: 2D nonlinear and non-dispersive long wave model (NLSW)	Single 80 m resolution Cartesian grid Bathy/topo: from BATNAS 90-140 m resolution data	Reconstructed from pre-/ post-collapse satellite observations with 0.24 km^3 volume (little detail given on definition of failure/slide geometry)

Table 1. Overview of main characteristics of earlier studies of the 2018 AK collapse and tsunami modeling.

Grid	Mesh size (*N, M*)	Resolution (m)	SW Corner (Lat., Lon.)
G1	3680,3900	50	-7°, 104.4°
G2	955, 1155	30 (horiz.) 7 σ (vert.)	-6.2357°, 105.2916°

Table 2: Parameters of grids used in simulations with NHWAVE (G2) and FUNWAVE (G1) (Fig. 1).

WG	Lon E. (Deg.)	Lat N. (Deg.)	Depth (m)	*t* meas. crest (s)	*t* meas. 1 cm (s)	*t* sim. crest (s)	*t* sim. 1 cm (s)
1.	105.4066^o	-6.1234^o	239.50	N/A	N/A	53-65	15.6-24.2
2.	105.3733^o	-6.1524^o	88.22	N/A	N/A	165.1-175.5	118.0-127.0
3.	105.4246^o	-6.0691^o	49.32	N/A	N/A	179-191	131.2-140.0
4.	105.4954^o	-6.1279^o	58.50	N/A	N/A	244.5-254.5	197.5-208.0
5.	105.3571^o	-6.1361^o	90.74	N/A	N/A	188.5-190.4	165.5-169.4
6.	105^o 50’ 15.0”	-6^o 11’ 21.5”	4.70	1980	1923	1995-2006	1967-1979
7.	105^o 57’ 10.8”	-6^o 01’ 02.5”	3.64	2700	2587	2712-2727	2617-2629
8.	104^o 37’ 08.5”	-5^o 30’ 01.2”	3.67	2520	2292	2550-2568	2358-2382
9.	105^o 19’ 06.1”	-5^o 28’ 08.7”	3.92	3600	3390	3660-3678	3564-3624

Table 3: Parameters of numerical wave gauges (WG) 1-9 (Figs. 1a,b): Lat-Lon, depth (in grids G1 (6-9) and G2 (1-5), assuming a MWL = MSL + 1.5 m, corresponding to the estimated average tide elevation at the time of the event), and arrival time (1 cm elevation or first main crest), measured/simulated range for 8 scenarios (Figs. 6,7; scenarios 1-8 in Table 4). WG 1-5 have no measured time (Fig. 6), but WG 6-9 are collocated with Tide Gauges (Fig. 10) at: (5) Serang, Marina Jambu, (6) Ciwandan, (8) Kota-Angung, (9) Panjang. In simulations, the AK collapse is assumed to take place at 20:57’ local time (UTC + 7). Simulated crest arrival times at 9 WG for 8 scenarios are within 2-18 s. Simulated differences in crest arrival time at tide gauges are 15-78 s, compared to the 1 minute data sampling interval. N/A: Not Applicable.

No.	Landslide rheology	Collapse Volume. (km^3)	Model MWL (m)
1.	Granular	0.313	MSL + 1.5
2.	Granular	0.272	MSL + 1.5
3.	Granular	0.224	MSL + 1.5
4.	Granular	0.175	MSL + 1.5
5.	Viscous	0.313	MSL + 1.5
6.	Viscous	0.272	MSL + 1.5
7.	Viscous	0.224	MSL + 1.5
8.	Viscous	0.175	MSL + 1.5
9.	Granular	0.224	MSL + 0.5
10.	Granular	0.224	MSL + 1.0
11.	Granular	0.224	MSL + 2.0

1211

1212 **Table 4:** Description of Anak's collapse scenarios simulated in the near-field with NHWAVE, each for
1213 420 s (Figs 3-8; see Table 5 for rheology parameters). For each scenario, FUNWAVE is initialized with
1214 NHWAVE results at 380 s, and simulations are performed fin the far-field or an additional 2 h (Figs. 9,
1215 10); MSL and MWL denote the mean sea level and mean water level, respectively. Scenarios 1-8 are the
1216 main collapse scenarios simulated and discussed in the paper, whereas scenarios 9-11 are additional
1217 simulations performed as part of the sensitivity analysis of model results to MWL detailed in
1218 Supplementary file #S3. Scenarios 3, 7, 9-11 correspond to the likeliest collapse volume of 0.224 km^3.
1219 Scenario 3, with the granular rheology, is deemed our likeliest collapse scenario.

1220

Granular collapse rheology			
Granular medium density	ρ_c	1,900	kg/m^3
Granular bulk density	ρ_{ac}	1,550	kg/m^3
Internal friction angle	$\emptyset_{ic}$	10	^{o}
Basal friction angle	$\emptyset_{bc}$	2	^{o}
Viscous collapse rheology			
Viscous fluid density	ρ_c	1,550	kg/m^3
Viscous fluid kinematic viscosity	υ_c	0.5	m^2/s

1221 **Table 5:** Parameters of granular landslide and viscous landslide collapse scenarios simulated with
1222 NHWAVE (see Table 4).

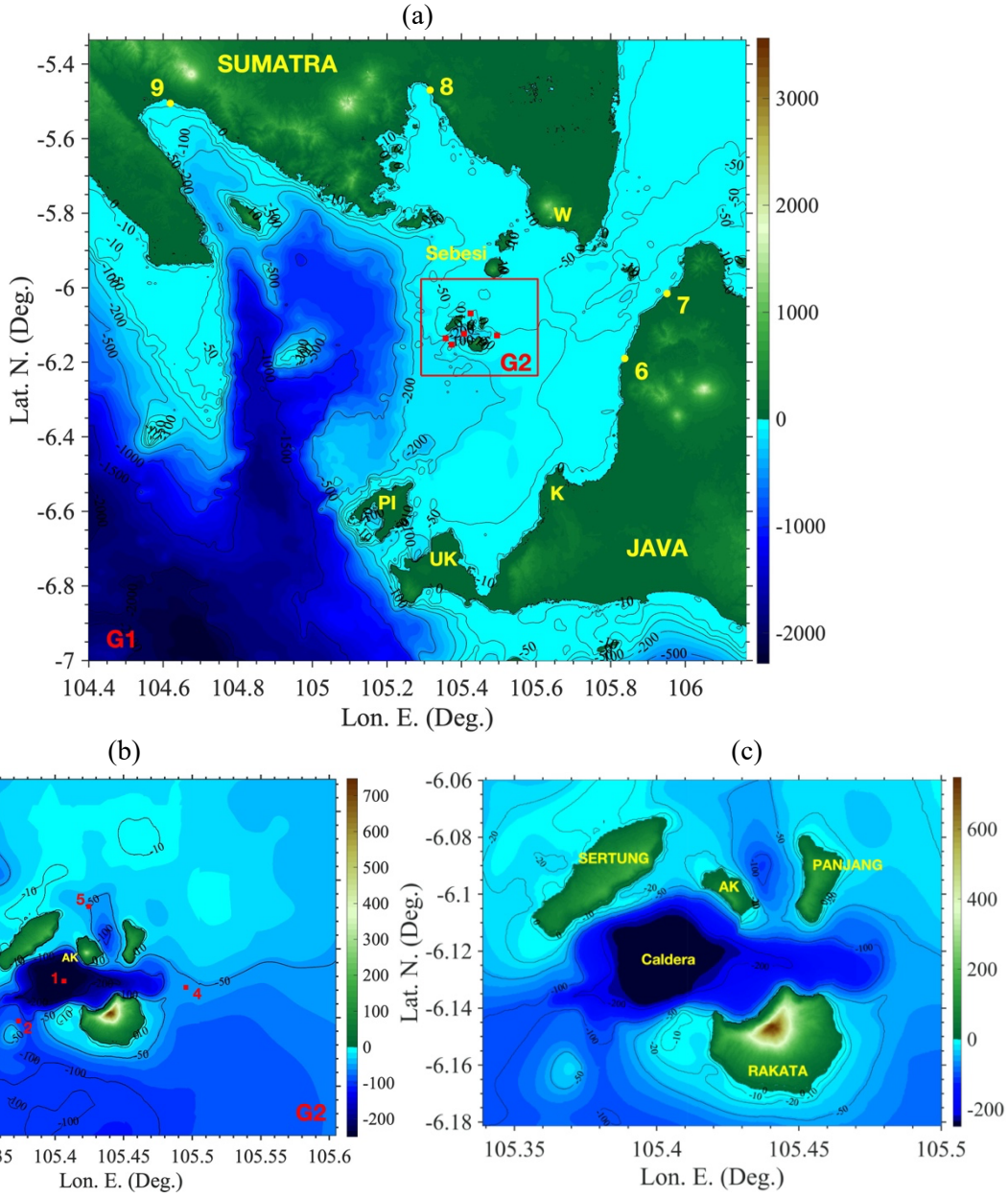

Figure 1: (a) Study area covered by 2D FUNWAVE 50 m Cartesian grid G1; (b) zoom-in onto 3D NHWAVE 30 m Cartesian grid G2 (red box in (a)), with 7 vertical σ layers, encompassing Anak-Krakatau (AK) and its surrounding islands (Rakata, Sertung, Panjang). Numbered symbols mark locations of numerical wave gauges (6-9 are collocated with tide gauges). Black contours and color scale is (a,b) pre- and (c) post-collapse (likeliest scenario) bathymetry/topography in meter, including an observed +1.5 m mean tide level. Letters in (a) are localities: (UK) Ujung Kulon; (K) Kolijaah; (PI) Panaitan Island; (W) Waymuli.

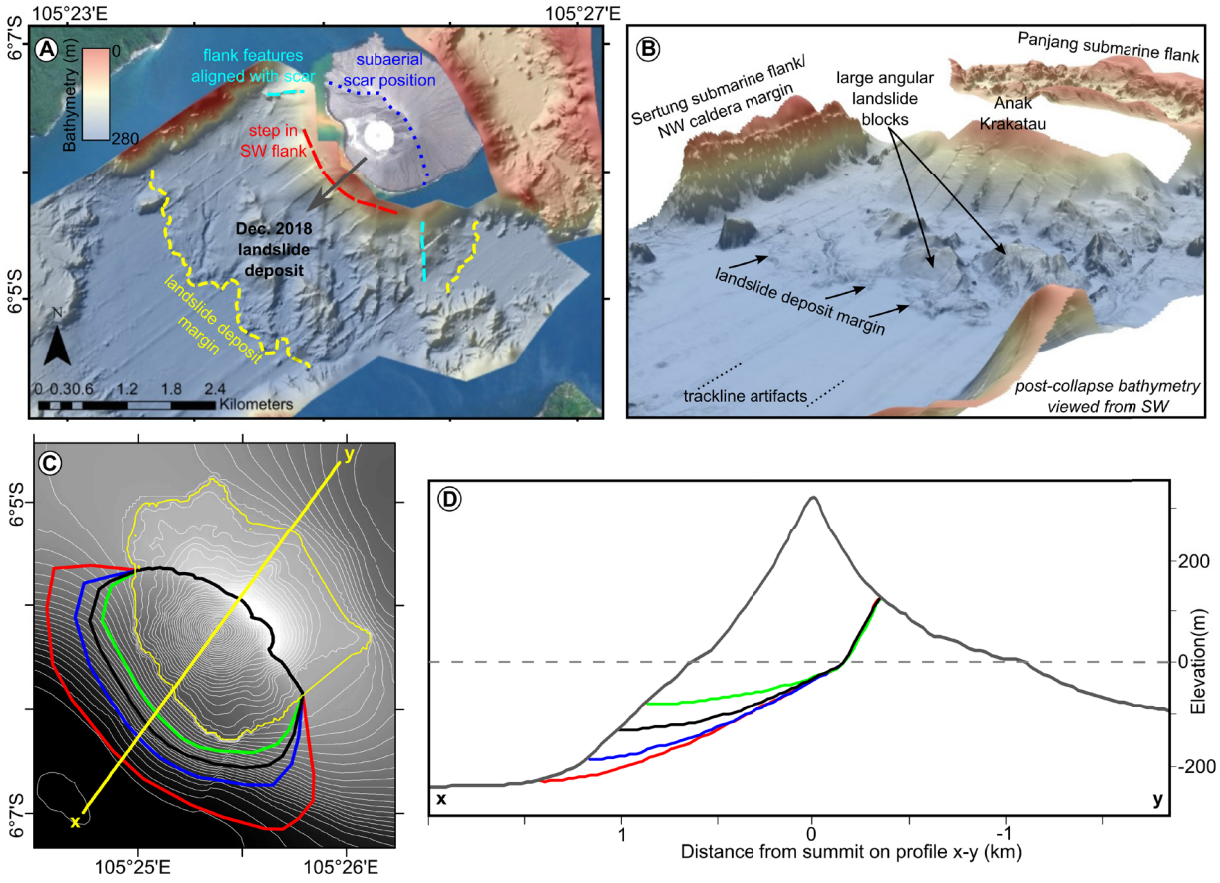

Figure 2: (a,b) Post-collapse bathymetry/topography of AK and surrounding islands (Fig 1) from August 2019 survey's seismic reflection profiles (Hunt et al., 2021), showing AK's subaerial scar and submarine landslide deposits; the rendering in panel (b) clearly shows large, blocky landslide deposits at the base of AK's SW flank. (c,d) Geometry of AK's four collapse scenarios modeled with NHWAVE, in (c) planview and (d) profile in SW direction (225 deg. to N; see trace in panel (c)), with colored lines marking the scenario of total collapse volume: (red) 0.313; (blue) 0.272; (black) 0.224 (deemed the likeliest volume scenario; see Figs. 1c and 3b and Table 4); and (green) 0.175 km^3. Yellow contour in (c) marks the post-collapse coastline and black line in (d) is AK's pre-collapse SW profile (culminating at 335 m).

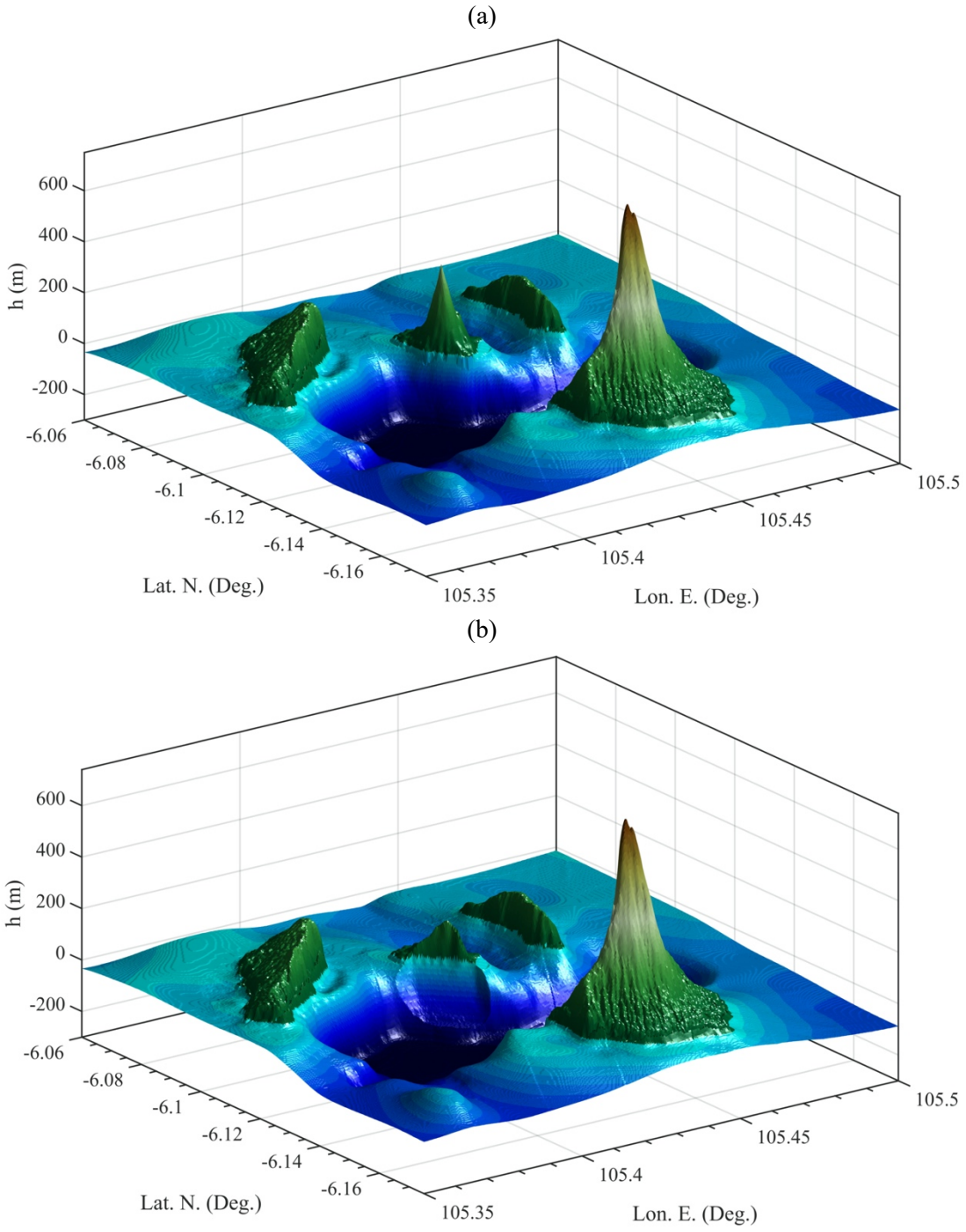

Figure 3: 3D view of composite pre- and post-collapse (likeliest scenario; #3 in Table 4) bathymetry/topography of AK and surrounding islands used in NHWAVE Grid G2 (Fig. 1c footprint), based on available pre-event data outside of Krakatau islands and August 2019 field survey data (see Fig. 2) in the caldera and surrounding islands (Hunt et al., 2021). There is a factor 10 vertical exaggeration.

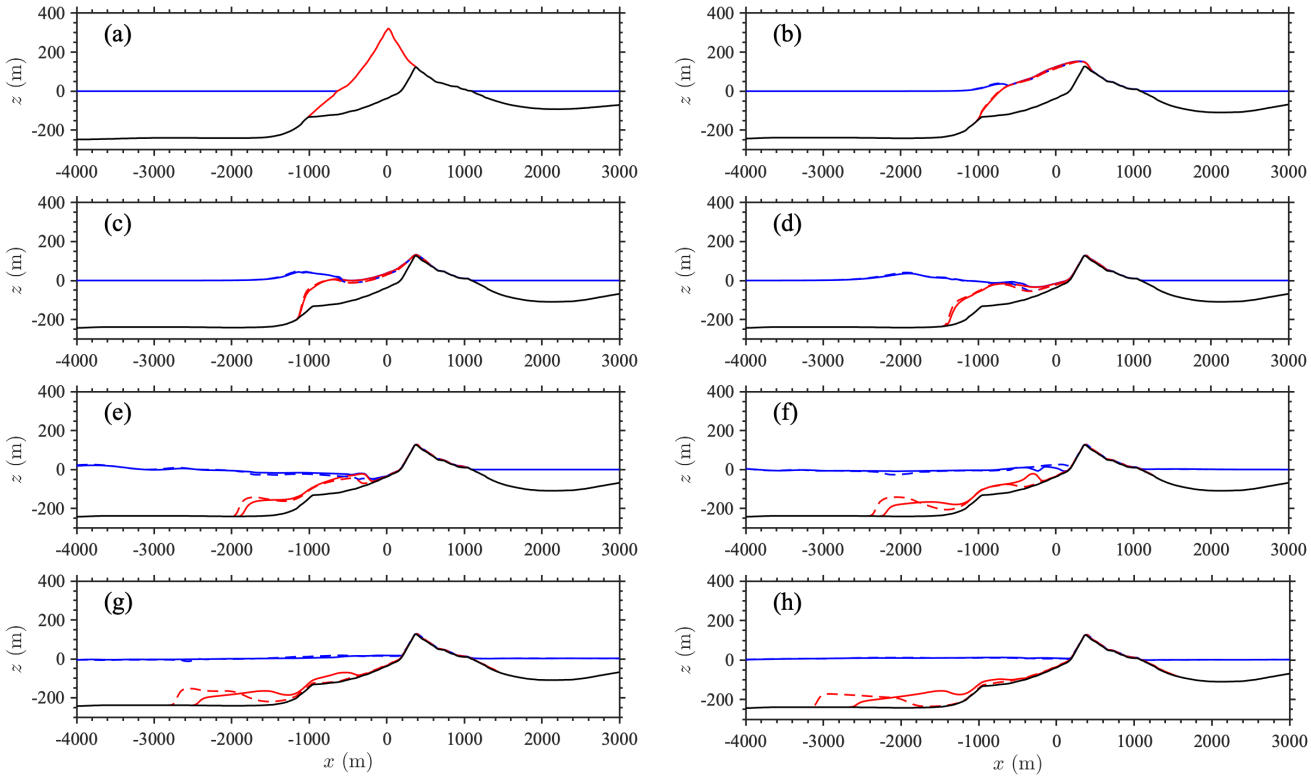

Figure 4: Simulation of likeliest AK collapse volume scenarios (with 0.224 km^3; #3 and 7 in Table 4) with NHWAVE in Grid G2 (Fig. 1) with a granular (solid; #3) or viscous (dashed; #7) rheology. Sub-panels show SW (225 deg. to north; Fig. 2) transects of computed instantaneous surface elevations (—/- - -) and slide profiles (—/- - -), at t = (a) 0, (b) 10, (c) 20, (d) 40, (e) 80, (f) 120, (g) 160 and (h) 200 s.

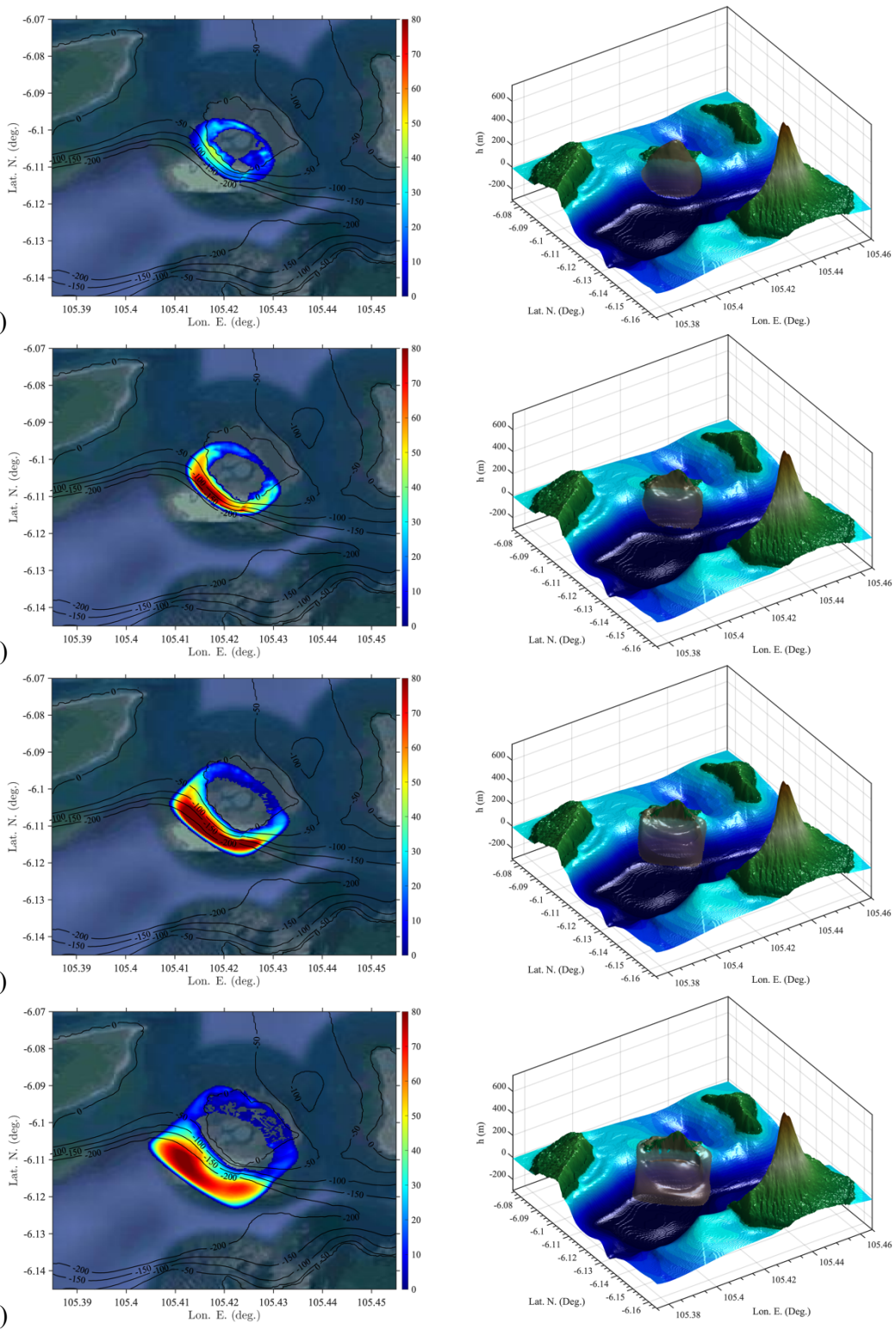

Figure 5: Snapshots of slide motion for granular case of Fig. 4 (#3 in Table 4), at t = (a) 10, (b) 20, (c) 40, (d) 80, (e) 120, (f) 160, (g) 200, and (h) 380 s. Color scale is slide thickness in meter. Contours are depth in meter.

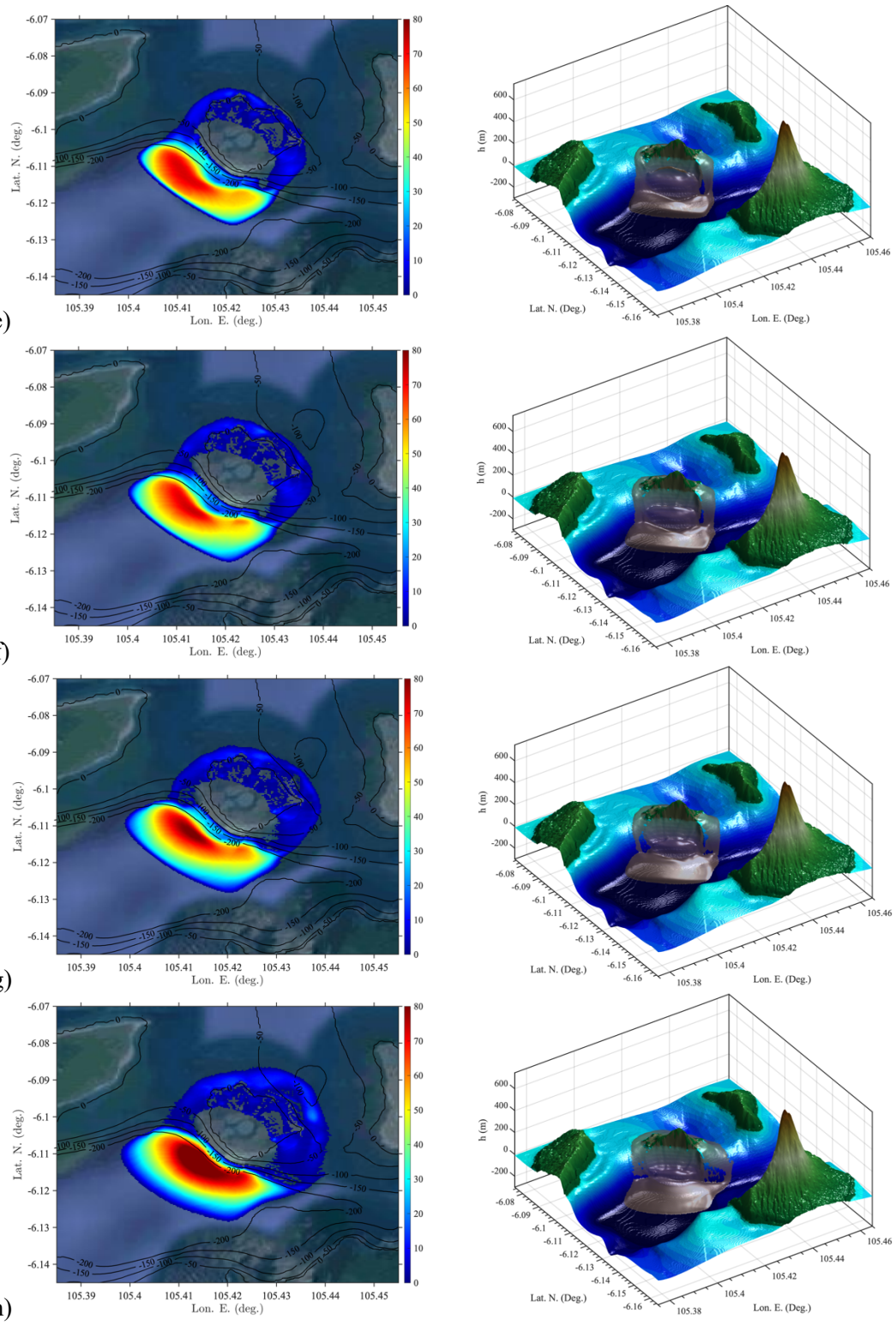

Figure 5: continued.

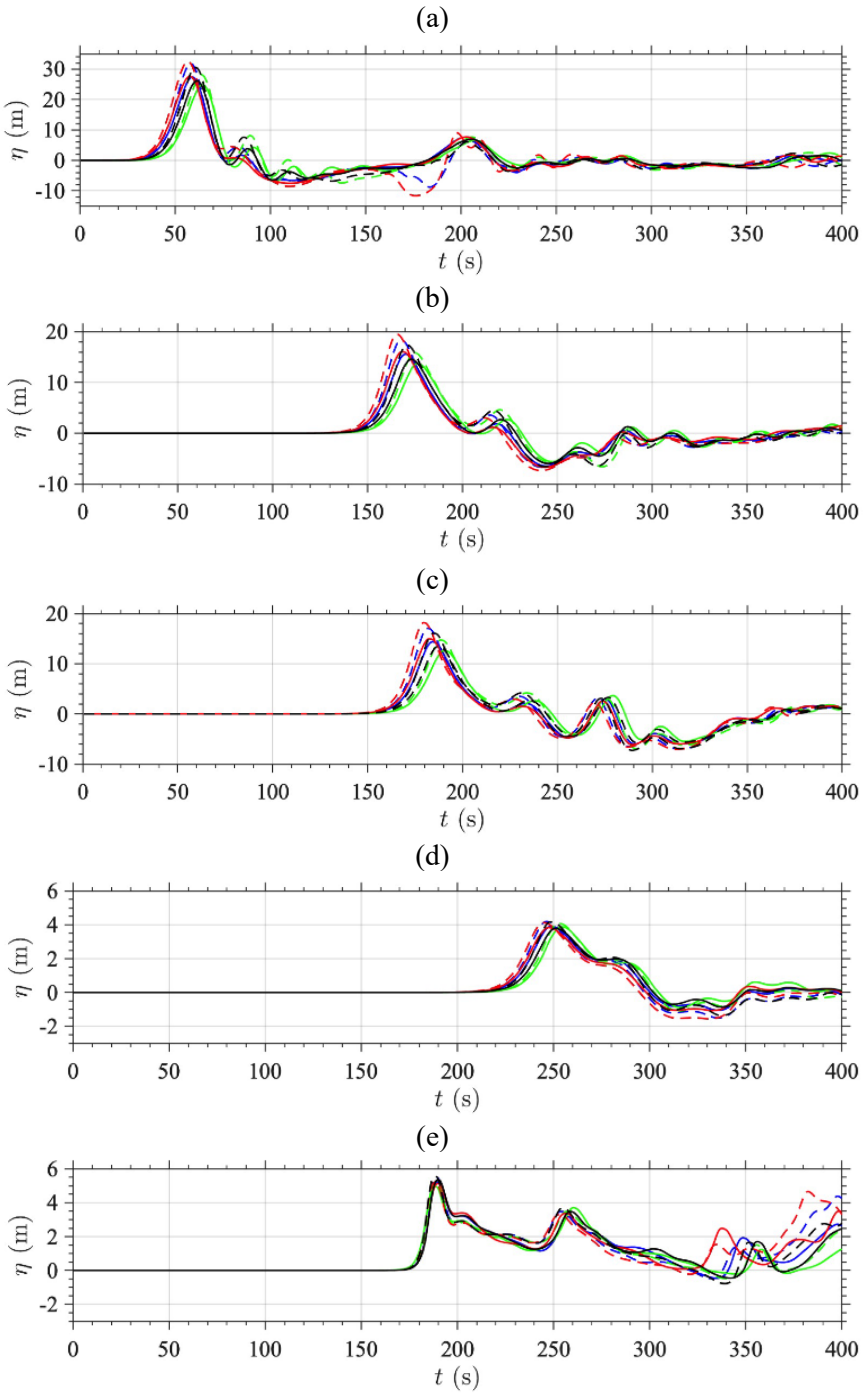

Figure 6: Time series of surface elevations computed at numerical wave gauges (WG) 1-5 (a-e; Fig. 1b) with NHWAVE in Grid G2 (Fig. 1), for 8 AK collapse scenarios (#1-8 in Table 4), with a granular (solid) or viscous (dashed) rheology, and volume (Figs. 2c,d): (—/- - -) 0.313; (—/- - -) 0.272; (—/- - -) 0.224 (likeliest scenario; see Figs. 1c and 3b); (—/- - -) 0.175 km^3. Time t = 0 is estimated collapse time, 20:57′ local time (UTC + 7). Note, reference level in simulations is MWL = MSL + 1.5 m (tide elevation).

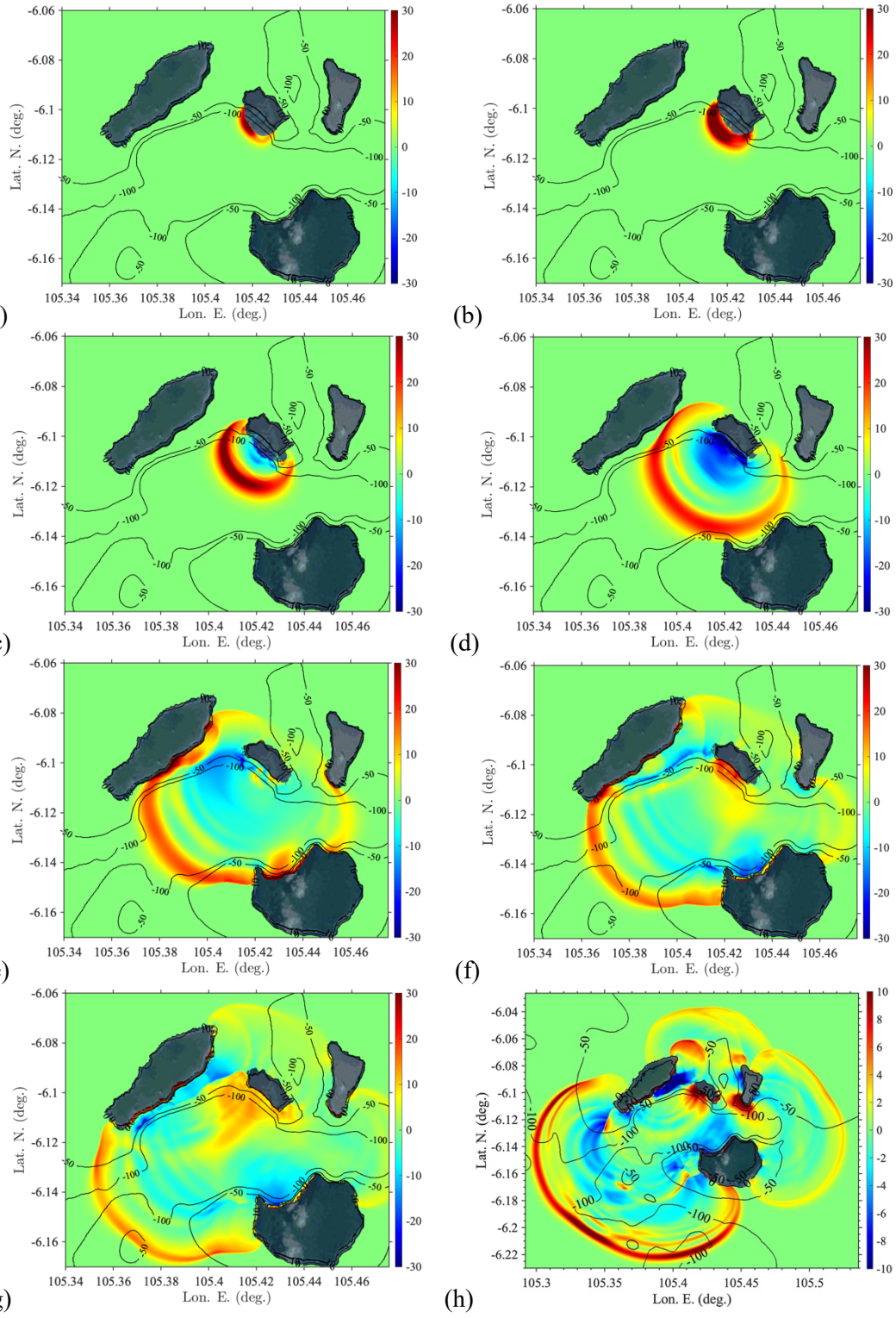

Figure 7: Snapshots of free surface elevations computed with NHWAVE in Grid G2, for likeliest collapse scenario (granular, 0.224 km^3; #3 in Table 4), at t = (a) 10, (b) 20, (c) 40, (d) 80, (e) 120, (f)160, (g) 200, and (h) 380 s (latter time is FUNWAVE initialization). Same case as Fig. 5. Reference level in simulations is MSL + 1.5 m.

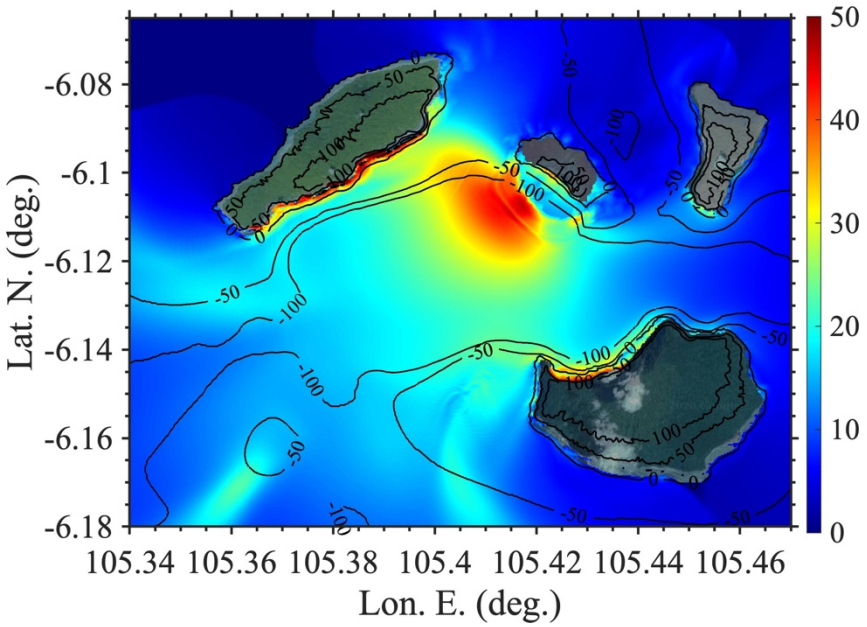

Figure 8: Maximum envelope of surface elevations computed with NHWAVE in Grid G2 for AK collapse likeliest scenario (granular, 0.224 km^3; #3 in Table 4), up to t = 420 s (color scale in meter). Reference level in simulations is MWL = MSL + 1.5 m.

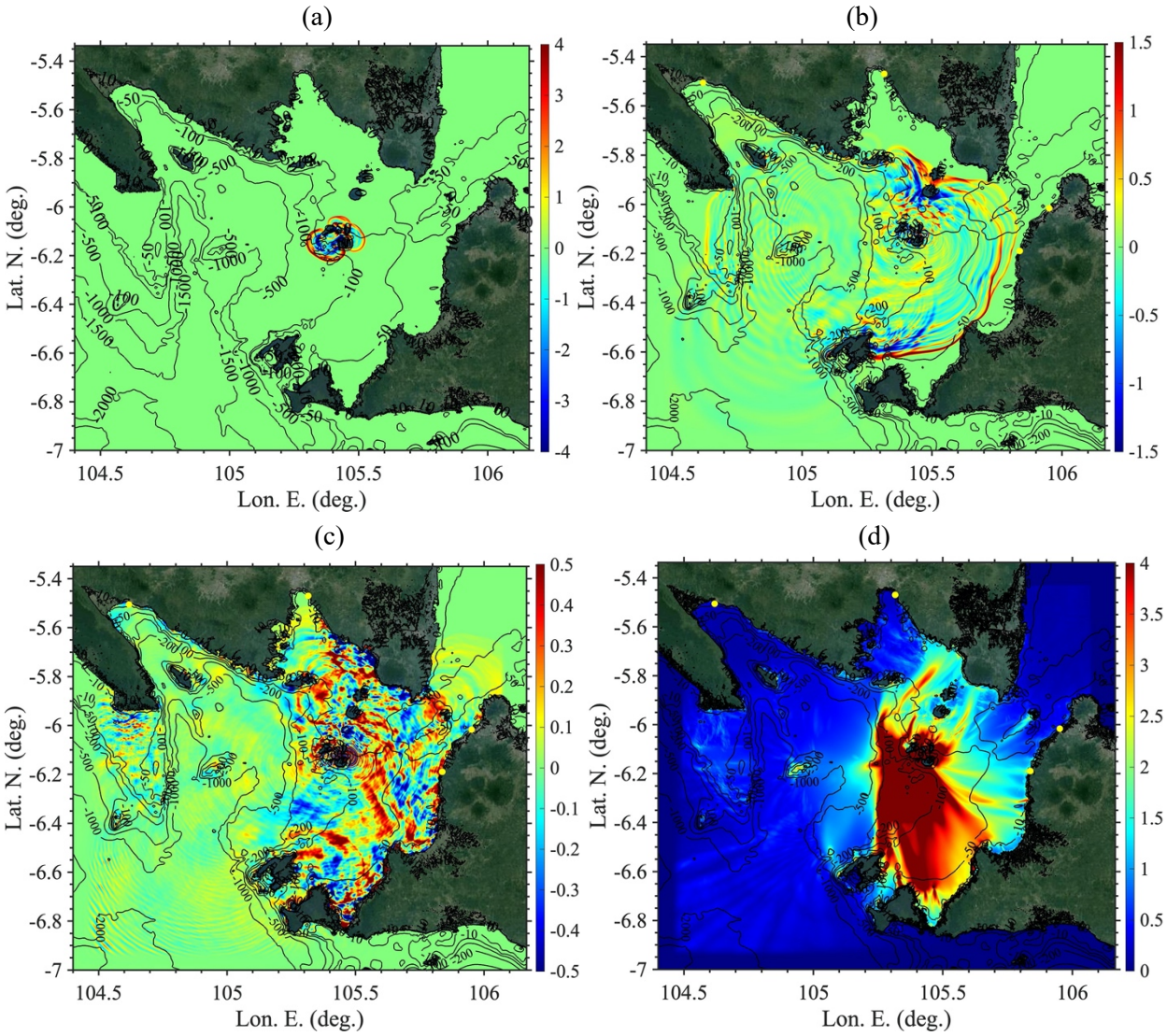

Figure 9: Tsunami surface elevations computed with FUNWAVE in Grid G1 for AK collapse likeliest scenario (granular, 0.224 km^3; #3 in Table 4). Initial elevation at t = (a) 380 s from NHWAVE simulation, (b) 1800 s, and (c) 3600 s; (d) envelope of maximum elevations up to t = 7,580 s (different color scales in meter). Maps show topography from Google Earth georeferenced satellite images embedded using an API key. Reference level in simulations is MWL = MSL + 1.5 m. Yellow bullets mark locations of tide gauges (see Fig. 1a).

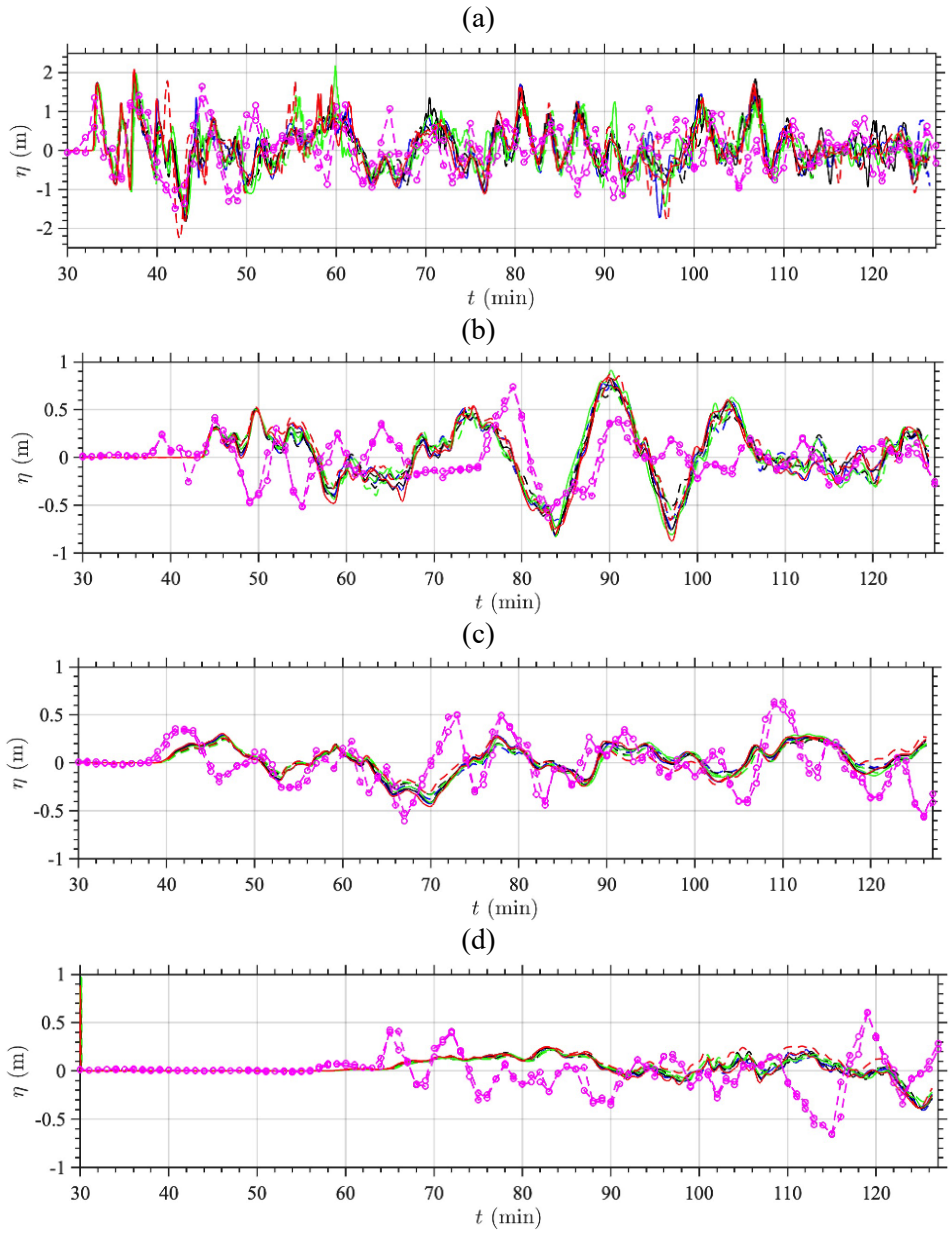

Figure 10: Time series of surface elevations, in simulations with respect to MWL = MSL + 1.5 m, at numerical wave gauges 6-9 (a-d; Fig. 1a), computed with FUNWAVE for 8 AK collapse scenarios (#1-8 in Table 4) with a granular (solid) or viscous (dashed) rheology, and volume (Figs. 2c,d): (—/- - -) 0.313; (—/- - -) 0.272; (—/- - -) 0.224 (likeliest scenario; see Figs. 1c and 3b); (—/- - -) 0.175 km^3, compared to collocated detided observations (-o-) with 2 sensors, at 4 tide gauges (Table 3). Time t = 0 is estimated collapse time, 20:57′ local time (UTC + 7).

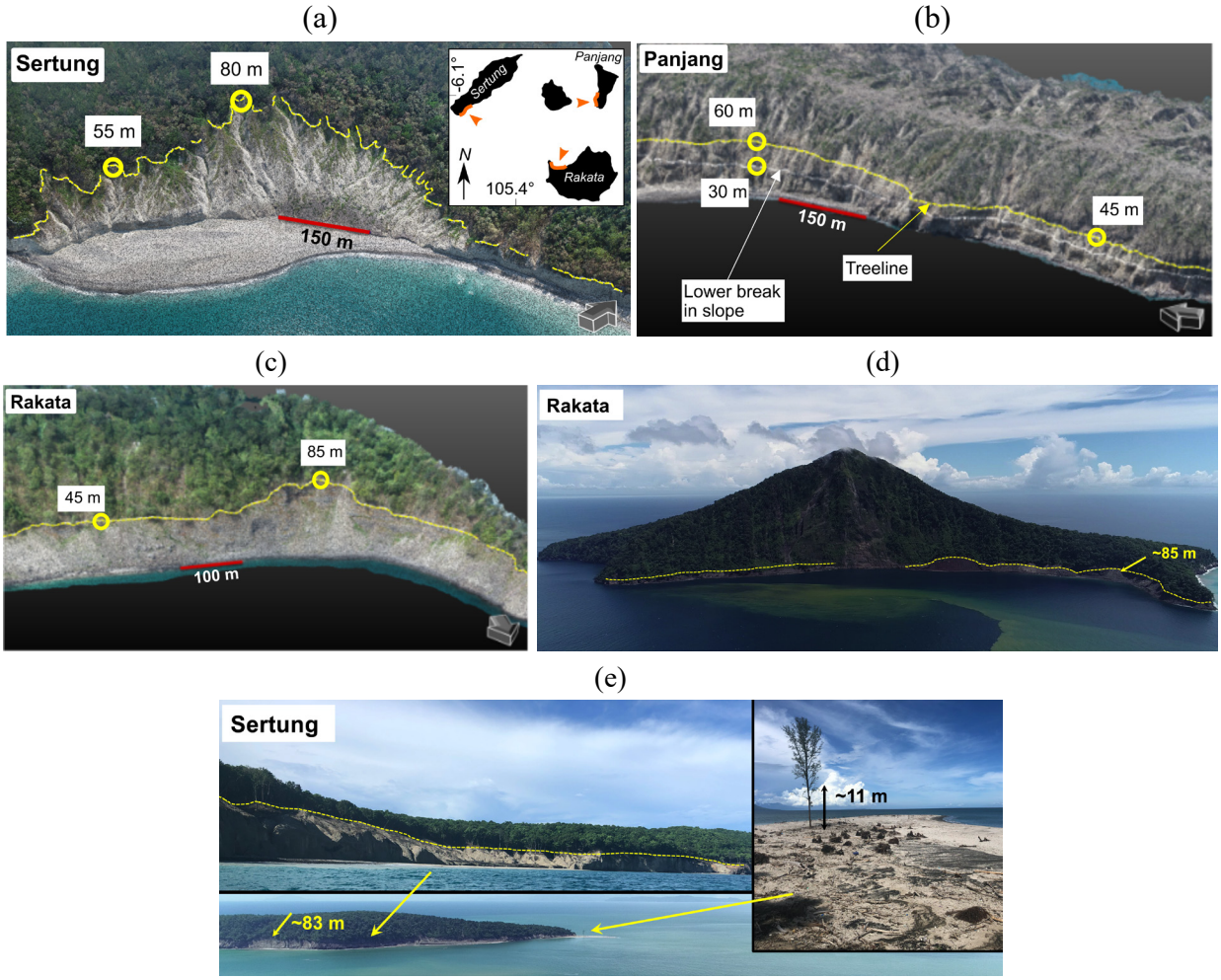

Figure 11: Pictures from AK field surveys of near-field runups (see Fig. 13 for actual elevations) on surrounding islands (Fig. 1c): (a,b,c) dashed yellow lines mark the authors August 2019 tree/vegetation line drone survey of Sertung, Panjang and Rakata, respectively (see inset in (a) for orientation); (d,e) Borrero et al.'s (2020) 02/2019 survey, of (d) Rakata's N/NW shore, (e) Sertung's SE/NE shore. In panel (b), the white dashed line marks the steepest slope limit on Panjang's W shore.

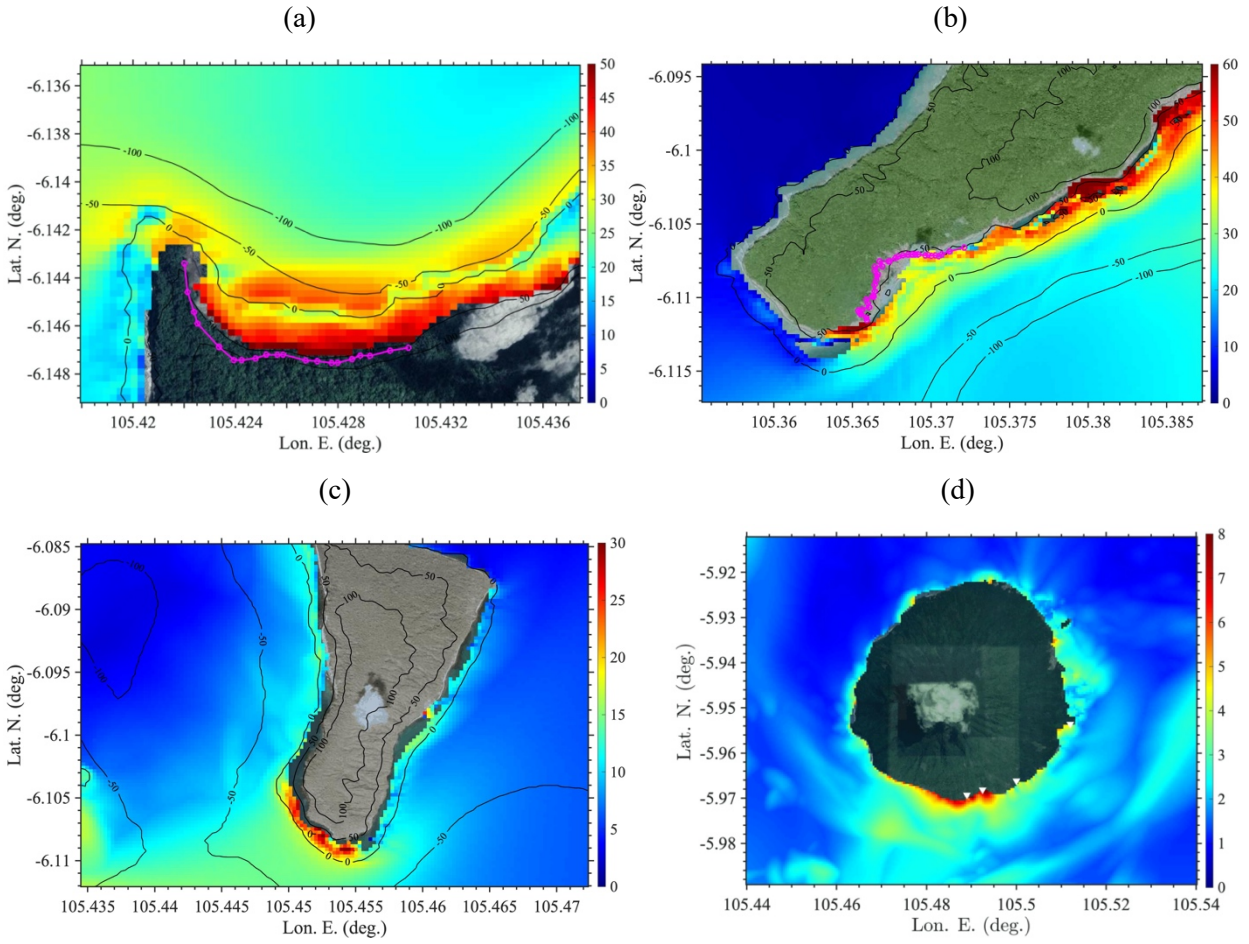

Figure 12: Zoom-in on maximum surface elevation (inundation) computed with (a-c) NHWAVE in Grid G2 (Fig. 8) or (d) FUNWAVE in Grid G1 (Fig. 9d) for the likeliest collapse scenario (granular, 0.224 km^3; #3 in Table 4), along (Figs. 1a,c): (a) Rakata's NW shore, (b) Sertung's SW shore, (c) Panjang's S shore, and (d) Sebesi. Pink circles/line in (a,b) indicate August 2019 drone survey (Figs. 11a,c); white triangles in (d) are flow depth/runup from Borrero et al.'s (2020) 02/2019 field survey of Sebesi (7.5, 9.0, 2.6, 2.0 m from W to E, respectively, referred here to MWL). Black contours are bathymetry/topography in meter. Note, reference level in simulations is MWL = MSL + 1.5 m (tide elevation).

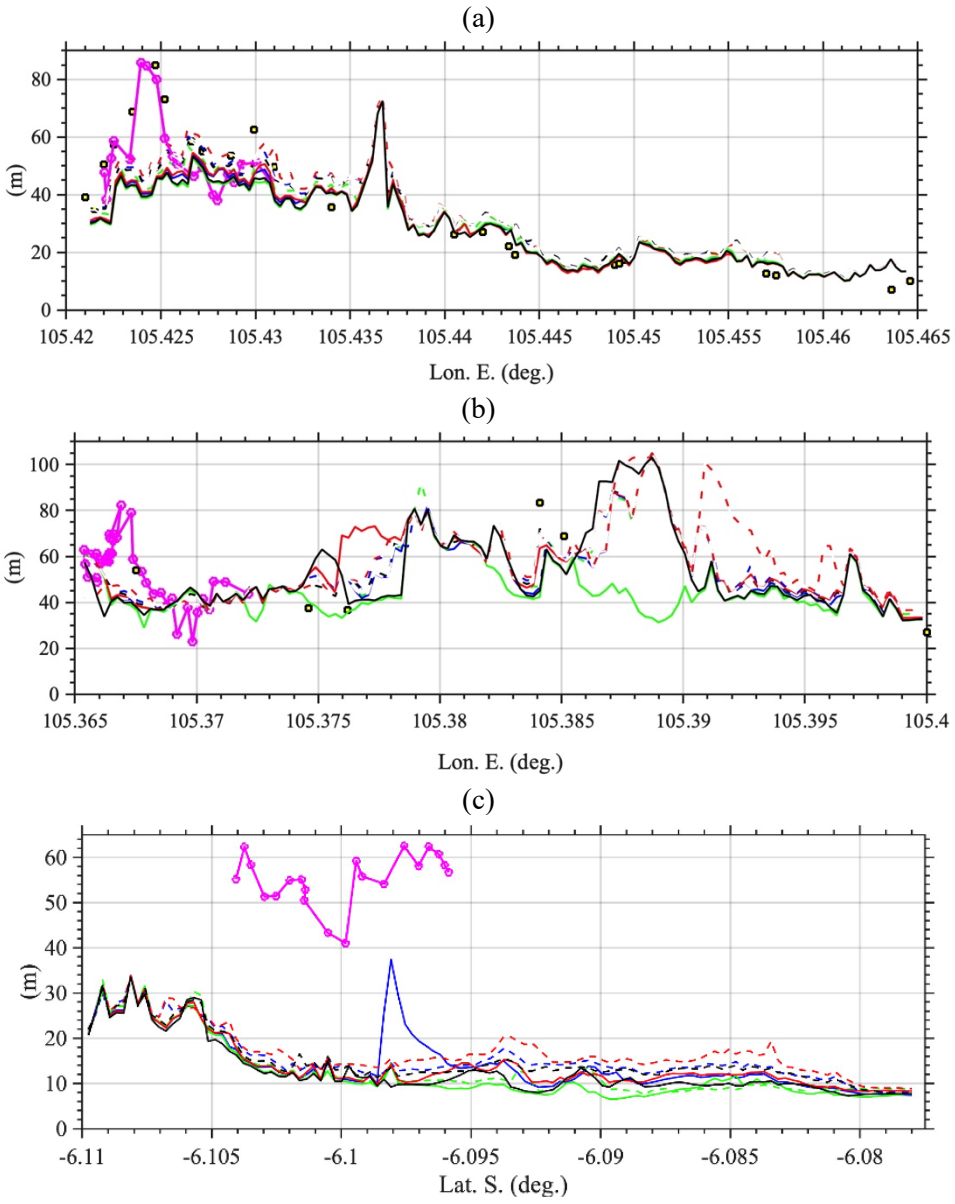

Figure 13: Maximum runup computed with NHWAVE along (Figs. 1c, 11, 12): (a) Rakata's N shore; (b) Sertung's S shore; and (c) Panjang's W shore, for 8 AK collapse scenarios (#1-8 in Table 4) with a granular (solid) or viscous (dashed) rheology, and volume (Figs. 2c,d): (—/- - -) 0.313; (—/- - -) 0.272; (—/- - -) 0.224 (likeliest scenario; see Figs. 1c and 3b); (—/- - -) 0.175 km^3, compared to the authors' August 2019 drone field survey (Fig. 11; -o-) of tree line and to the field measurements (yellowed squares) of Borrero et al. (2020); note, the latter authors reported an 8 m flow depth for north of Panjang. Note, in simulations and the field data, zero elevation is MWL = MSL + 1.5 m (tide elevation).

(a) (b) (c)

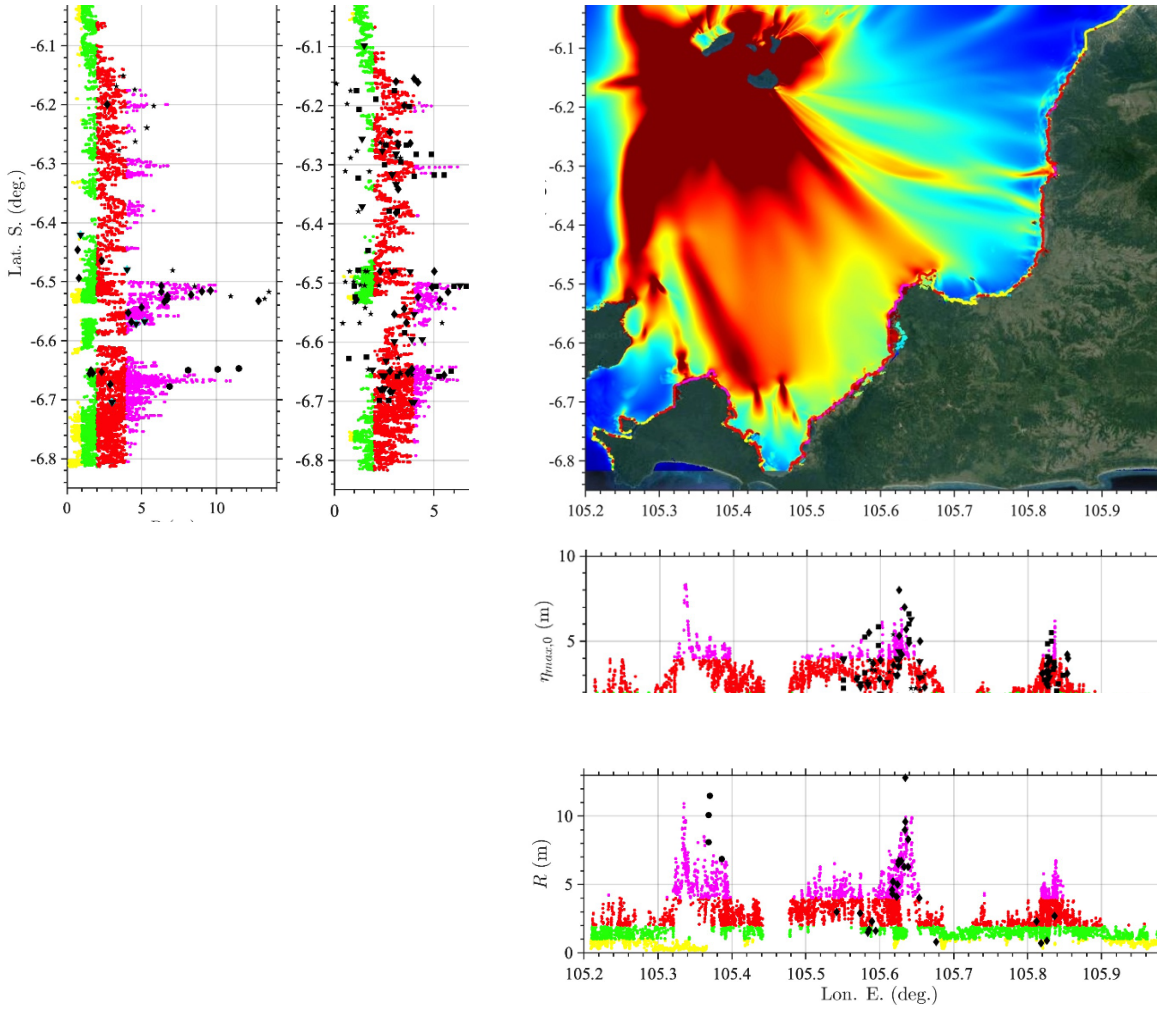

Figure 14: (a,e) Maximum Runup R, and (b,d) flow depth at the shore $\eta_{max,0}$ (along 0 m contour) from (a) maximum envelope of surface elevation computed with FUNWAVE in Grid G1, for likeliest AK collapse scenario (granular, 0.224 km^3; #3 in Table 4; Fig. 9d) zoomed-in on Java; for clarity, 4 classes of elevations are defined: (•) 0-1 m; (•) 1-2 m; (•) 2-4 m, and (•) > 4 m. Results are compared with field measurements of flow depth and runup, from: (■) TDMRC (2019), (★) Muhari et al. (2019), (♦) Putra et al. (2020), (▼) Heidarzadeh et al. (2020b), and (●) Borrero et al. (2020) surveys.

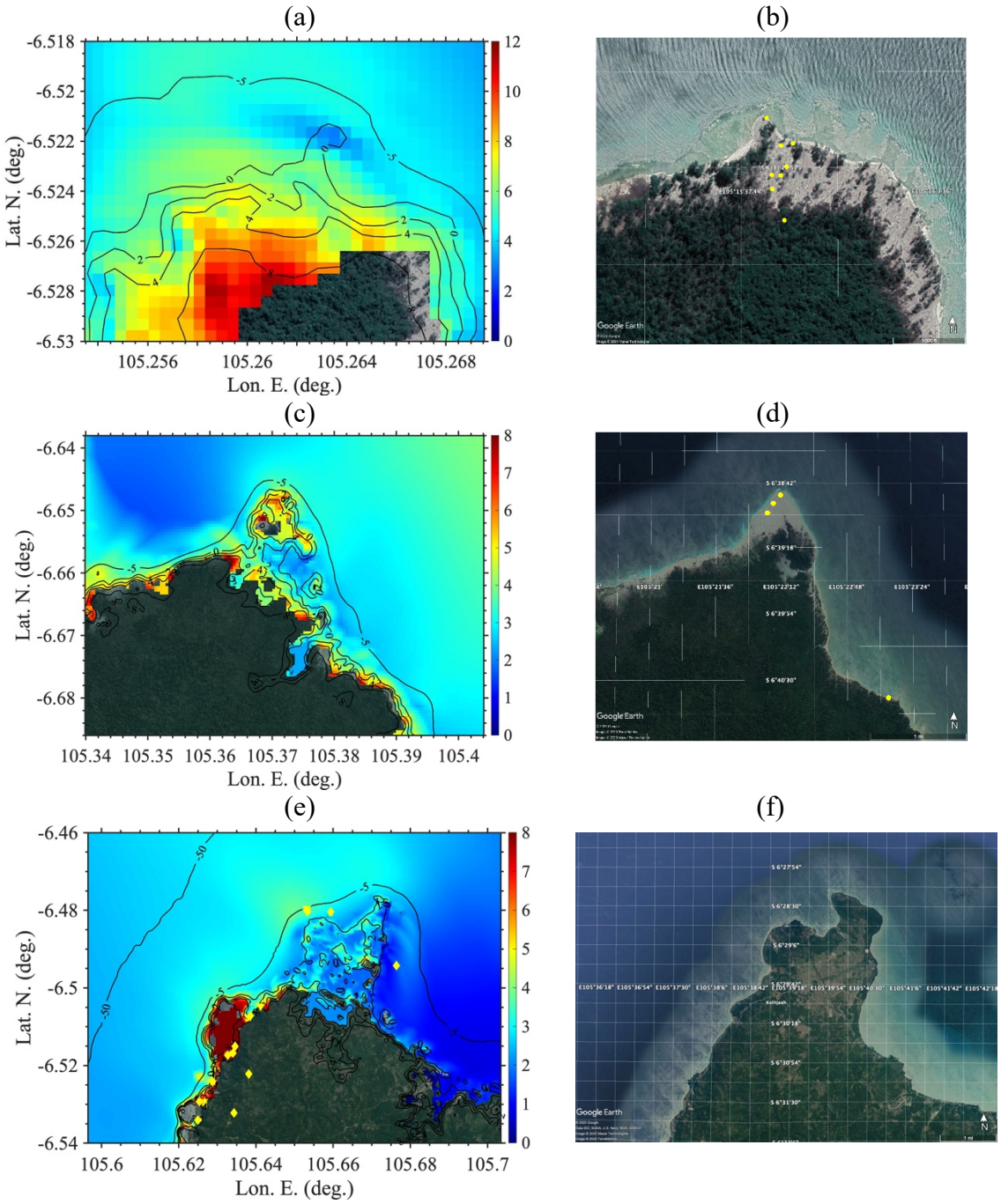

Figure 15: (a,c,e) Max. surface elevation (FUNWAVE, Grid G1; color scales in meter), for likeliest AK collapse scenario (granular, 0.224 km^3; #3 in Table 4; Fig. 9d), zoomed on (Fig. 1a): (a) Panaitan Island (PI); (c) Ujung Kulon (UK); and (e) Kolijaah (K). (b,d,f) Google Earth image of PI, UK and K (11/20). (•) in (b,d) are locations of Borrero et al.'s (2020) elevation survey, measured from N to S, in (b) at (around Lon. E. 105.2622): 6.4, 7.3, 6.5, 6.1, 8.4, 6.4, 6, 7.4 m (MWL) (note southern point was missing a terrain correction that was added), and in (d) at: 11.5, 11.1, 8.1, 6.9 m (MWL). Black contours in (a,c,e) are bathymetry/topography in meter and color scale is maximum surface elevation in meter.

(a)

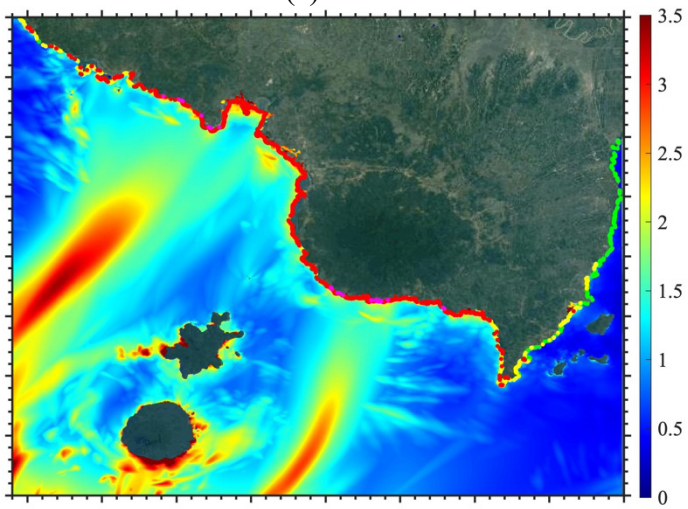

(b)

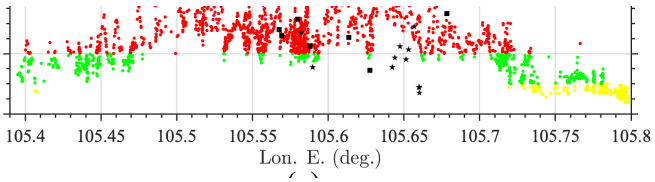

Figure 16: Same results as in Fig. 14: (a) Envelope of maximum surface elevation (FUNWAVE, Grid G1; color scales in meter), for likeliest AK collapse scenario (granular, 0.224 km^3; #3 in Table 4; Fig. 9d), zoomed on Sumatra (Fig. 1) with 4 classes defined as: (•) 0-1 m; (•) 1-2 m; (•) 2-4 m, and (•) > 4 m; (b) comparison of computed flow depth at the shore with field surveys of: (■) TDMRC (2019), (★) Muhari et al. (2019); (c) View of Waymuli (W, Fig. 1a, 105.6348 E), looking east, from Fritz et al. (2019) 02/2019 field survey.